Chapter 4

HB Dynamics in a Double Minimum System

The previous section focussed on the description of hydrogen bond dynamics in a system whose PES is characterized by a single minimum with pronounced anharmonic couplings. Vibrational excitation within the electronic ground state was studied, and it was demonstrated that the displacement of the hydrogen atom triggers the motion of the molecular skeleton.

We now turn to systems whose potential energy surface is marked by a double minimum, corresponding to structures X-H$\cdots$Y and X$\cdots$H-Y. There are two motivations for the following study: First, the PES for a double minimum system can be expected to be even more anharmonic than for a single minimum system. The question arises which methods are suitable to deal with such a situation. Second, given the understanding of the dynamics and the possibility to apply ultrafast IR laser pulse one might ask whether it is possible to drive the hydrogen atom from the proton donor, X, to the proton acceptor, Y by using suitable IR laser pulses, for example. As has been already mentioned, the hydrogen atom couples to other molecular degrees of freedom, so IVR might compete or even disable the control. In order to realize the control, the hydrogen bonded system should have a low barrier for two reasons: (i) in order to stay in the region of lower density of states (high barriers would increase the probability of involvement of a rather large number of modes); (ii) the system would be provided with less energy during the interaction with the external field (which decreases the probability of energy loss from the reaction coordinates). In addition, the potential should be asymmetric so that the reactants can be distinguished from the products [98].

In the following, we will present a model study for a double minimum system, i.e., Salicylaldimine [99] - [101]. We will contrast the AFF and the CRS method and use the latter to unravel the complex IR absorption spectrum by means of laser driven nuclear wave packets. Eventually, we will draw some conclusions concern-

ing the controllability of this system.

4.1 Model System Salicylaldimine

A suitable system for investigation of a hydrogen transfer reaction would be the one that contains a relatively weak intramolecular hydrogen bond, like 2-hydroxybenzaldimine compounds, Fig. 4.1. The two stable tautomeric forms are *enol* and *keto* with the hydrogen being attached to the oxygen and the nitrogen atom, respectively. We investigated the simplest member of this family, Salicylaldimine (SA), where the R group is simply the hydrogen atom. The choice was made according to the fact that the smallest computational effort is required for performing the quantum chemistry calculations for this molecule, since the numerical effort increases significantly with the enlargement of the R group. Quantum chemical investigations, e.g., optimized structures of SA have already been reported, [102] - [105]. Earlier investigations concerning this tautomerization reaction showed that this is not a hydrogen, but rather a proton transfer reaction [105]. Keeping this in mind, we will use the more general term *hydrogen transfer* in the following.

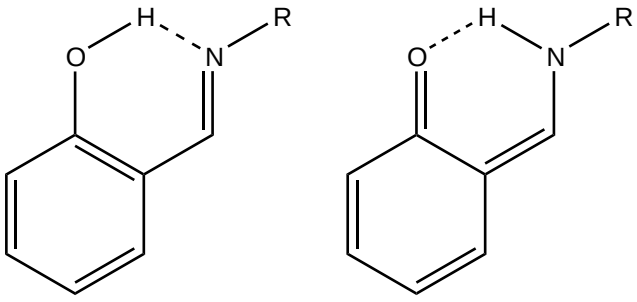

enol keto

Figure 4.1: The enol form of the 2-hydroxybenzaldimine compounds (left) and the keto tautomer (right).

4.2 Exploring the Enol Well in SA with the AFF Method

The Anharmonic Force Field approach (described in Section 2.2.1) has been used for obtaining the linear IR spectrum of Salicylaldimine in order to study the PES in the proximity of the global minimum. That is, we investigated the properties of the enol tautomer.

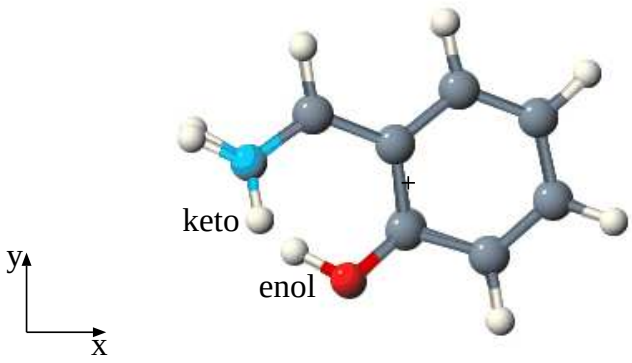

Figure 4.2: The stationary points (enol and keto form) of Salicylaldimine overlayed. The origin of the coordinate system, marked by a plus sign, coincides with the center of mass. The molecule lies in the (x, y) plane, with the axes pointing along the principal axes of inertia of the enol tautomer.

The structures of the two tautomers were optimized using the B3LYP functional and a 6-31+G(d,p) basis set and they are shown superimposed in Fig. 4.2. Both tautomers are planar, as is the transition state (not shown).

The experimental spectra of N-phenylsalicylaldimine in CCl_4 are shown in Fig. 4.3 [106]. This molecule is slightly different from SA: the R group is here *Ph* instead of *H*. Nevertheless, the hydrogen atom that forms the hydrogen bond is separated from the R group. That is, the phenyl group (or in general - the R group) should not have significant influence on the hydrogen motion. In other words, we expect the spectra of N-phenylsalicylaldimine and Salicylaldimine to have similar properties in the regions which are relevant for the present investigation (modes that mainly involve motion of the reactive hydrogen atom). However, the nature of the R group affects the skeleton modes, leading to a substructure that is rather different for different molecules. Therefore, we are not comparing the total spectra including the fine structure, but rather focus on the position of the OH bending and stretching vibration. The black and the blue lines on Fig. 4.3 correspond to the protonated and the deuterated species, respectively. Different spectral regions are shown on the upper and the lower Panel. The OH bending vibration lies around 1400 cm^{-1} (upper Panel), while the OD bending mode is red shifted and is centered around 1050 cm^{-1}. Concerning the stretching region (lower Panel) the OH stretching band is spread from 2500 to 2900 cm^{-1}, and the OD stretching band between 2000 and 2300 cm^{-1} The difference in the two spectra arises from the different frequencies of the normal modes that include the H and the D atom. Besides the obvious changes with respect to the OH/OD bending and stretching vibration,

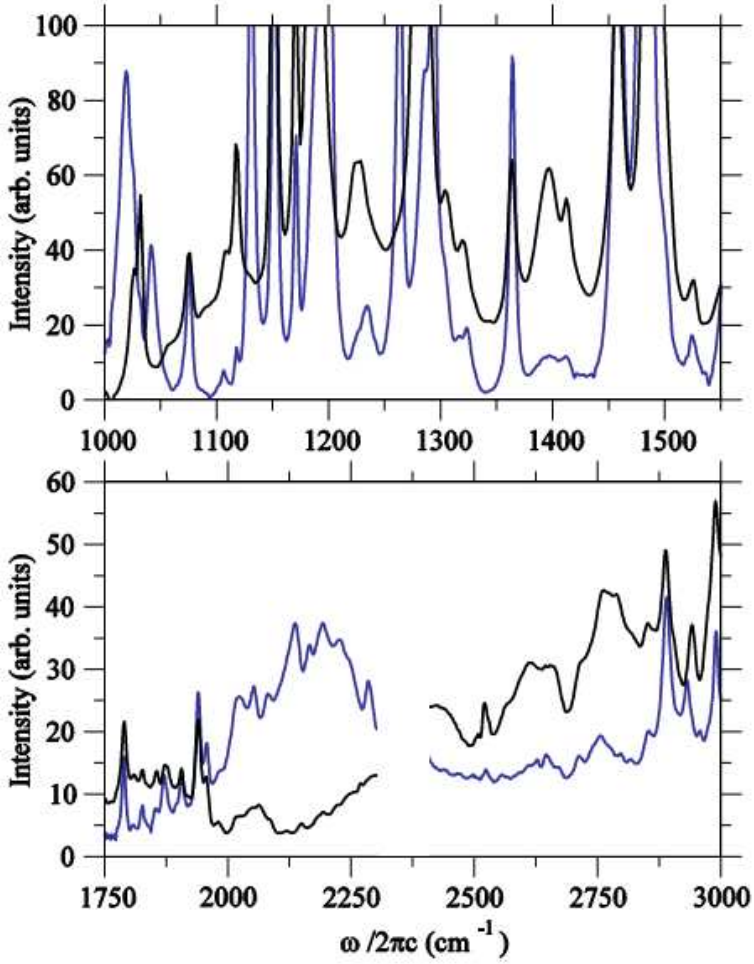

Figure 4.3: Experimental spectra of N-phenylsalicylaldimine in CCl_4. The upper Panel covers the region of the OH/OD bending, and the lower of the OH/OD stretching vibration. In both cases, the black/blue line corresponds to the protonated/deuterated species. The data in the interval 2300 - 2400 cm^{-1} have been omitted since they are not reliable, due to the difficulties during the measurements [106].

other degrees of freedom are affected by deuteration which results in the red or blue shift of the corresponding bands, change in their intensity and appearance or disappearance of certain peaks (for instance, notice the emerging of the peak around 1260 cm^{-1}).

Since we are interested in the hydrogen bond dynamics, the emphasis was put on the OH (OD) bending and the OH (OD) stretching vibration and their coup-

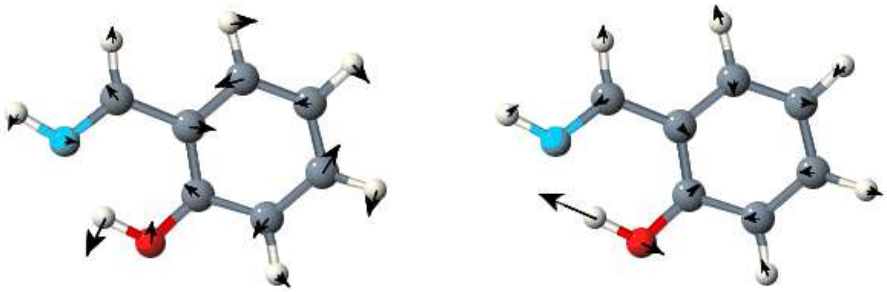

ν_b ν_s

Figure 4.4: The OH bending (ν_b) and stretching (ν_s) vibration of SA.

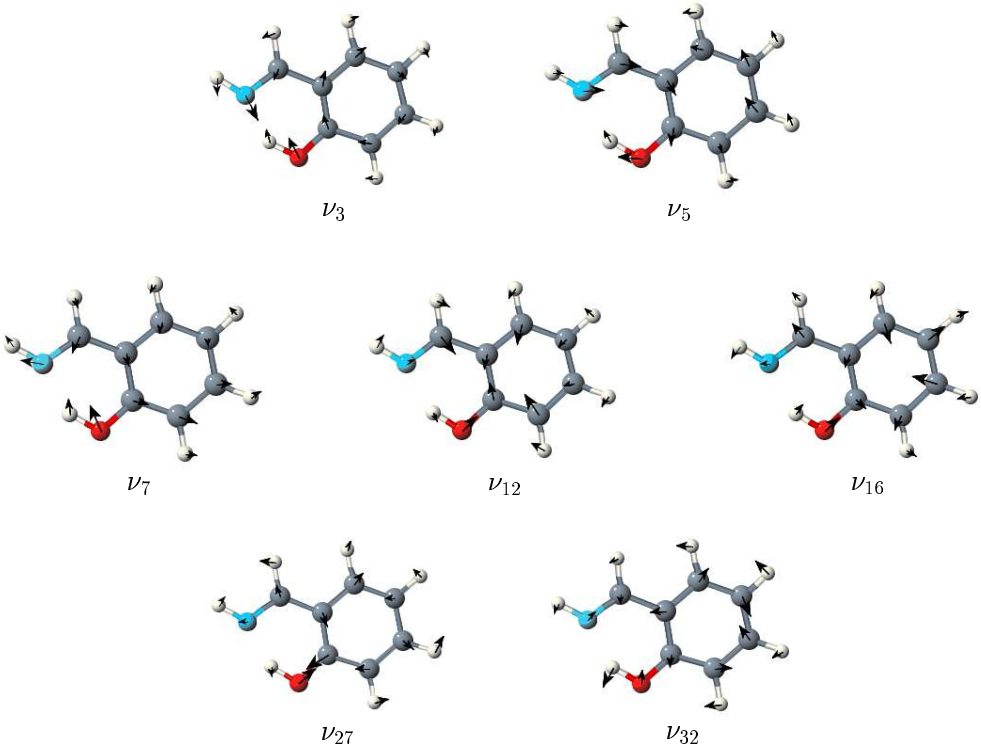

ν_3 ν_5 ν_7 ν_{12} ν_{16} ν_{27} ν_{32}

Figure 4.5: The in plane normal mode vibrations that (according to the computed cubic and quartic anharmonic terms) strongly couple to the OH bending and the OH stretching vibration.

i	ν_b	ν_s	ν_3	ν_5	ν_7	ν_{12}	ν_{16}	ν_{27}	ν_{32}
ω_i (cm^{-1})	1457	3156	288	426	470	764	880	1328	1536

Table 4.1: Harmonic values of the mode frequencies at the enol configuration of SA that correspond to modes displayed in Fig. 4.4 and 4.5.

ling to the skeleton normal modes. These two *significant* vibrational modes are displayed in Fig. 4.4.

In order to identify the molecular degrees of freedom that couple to the hydrogen motion, we computed the cubic and the quartic anharmonic terms (cf. Section 2.2.1) and considered only those modes that represent the *in plane* motion. Namely, the optimized structure of the enol tautomer is planar, due to the presence of the aromatic ring, and since the OH bending and stretching vibrations also take place in the plane of the molecule we disregarded the out of plane vibrations. Although the OH out of plane bending vibration might also be coupled to the two main modes of interest, inclusion of out of plane modes would result in a model of rather high dimensionality whose investigation would require a large amount of CPU time.

By examining the 3$^{\text{rd}}$ and the 4$^{\text{th}}$ derivatives of the potential with respect to ν_b and ν_s, seven additional degrees of freedom have been identified to couple to the hydrogen motion. All of them are characterized by (relatively) large displace-

i, j, k	$k_{i,j,k}$ in cm^{-1}
s, s, s	-2783
s, s, 3	373
b, s, s	349
s, s, 5	-217
s, s,32	180
b, b, s	168
s, s, 7	149
b, s,32	128
b, b, b	-99
s,32,32	98
b, s,27	77
s, s,12	-75
s, 3, 3	-72
b, s, 7	68
s,27,32	57
s, 7,32	56
b, b,32	-52
b, s, 5	-47
b, s,12	-45

i, j, k	$k_{i,j,k}$ in cm^{-1}
s, s,16	-44
b, b,27	-38
s, 5,32	-36
b, s, 3	-36
s, 3, 5	34
s, 5,27	-34
s,12,32	-31
b, 7, 7	-29
b, b, 3	-27
s, 3,27	26
b, b, 7	-26
s, 3, 7	-25
s, s,27	-24
s, 7,27	24
b, b,12	-23
s, 7, 7	23
b, 3, 7	-22
b, 7,32	-22
b, b, 5	20

Table 4.2: Significant cubic anharmonic terms that involve ν_b and ν_s, with $k_{i,j,k} = \frac{\partial^3 V}{\partial Q_i \partial Q_j \partial Q_k}$.

i, j, k, l	$k_{i,j,k,l}$ in cm^{-1}
s, s, s, s	1752
b, s, s, s	-227
b, b, s, s	-201
s, s, s, 3	-162
b, s, s,32	-159
s, s, s,32	-136
s, s, s, 5	117
s, s,32,32	-114
b, s, s, 5	92
b, b, b, s	77
b, s, s,27	-77
s, s,27,32	-68
s, s, s,12	66
s, s, 5,32	61
b, b, b, b	54
s, s, s, 7	-53
b, s, s,12	49
b, b, s,32	46
s, s,12,32	46
b, s, s, 7	-44
b, b, s, 3	43
b, b,32,32	43

i, j, k, l	$k_{i,j,k,l}$ in cm^{-1}
b, b, 3, 3	-41
b, b, s, 5	-40
b, s, 3, 3	-39
s, s, 5, 7	38
s, s, 5,27	37
s, s, 7,32	-36
s, s, 7,27	-34
b, s,32,32	32
b, b, b,32	28
s, s, 3,32	-28
b, s, 5,32	-26
b, s, 3,32	26
b, b, 7,32	25
s, s, s,16	25
s, s, 5, 5	-25
b, b, 3, 7	22
b, s, 3,12	-22
b, s, 3,16	21
b, s, 5, 7	-20
s, s,12,27	17
b, b, s,27	16
b, s, s, 3	-15

Table 4.3: Significant quartic anharmonic terms that involve ν_b and ν_s, with $k_{i,j,k,l} = \frac{\partial^4 V}{\partial Q_i \partial Q_j \partial Q_k \partial Q_l}$.

ments of the oxygen atom. Normal mode displacements of those seven modes are shown in Fig. 4.5, the harmonic frequencies are compiled in Table 4.1, and some of the cubic and quartic anharmonic terms are given in Tables 4.2 and 4.3, respectively. The anharmonicity along the ν_s mode is reflected in high values for $k_{s,s,s}$ and $k_{s,s,s,s}$. Large values of $k_{b,s,s}$ and $k_{s,s,3}$ suggest that the stretching vibration is considerably modified through interactions with ν_b and the low frequency mode ν_3.

According to the expression for the potential energy operator, Eq. 2.42, the Hamiltonian is given by (cf. Eq. 3.2)

$$H_{\mathrm{AFF}} = \sum_i T_i + V^{(1)}(\mathbf{Q}) + V^{(2)}(\mathbf{Q}) + V^{(3)}(\mathbf{Q}) + V^{(4)}(\mathbf{Q}) \qquad (4.1)$$

where $\mathbf{Q}$ comprises the nine degrees of freedom.

Nine normal modes form 165 cubic and 495 quartic anharmonic terms. For the present calculations, we included all cubic anharmonicities, the diagonal quartic terms, the quartic terms that couple ν_b and ν_s, two - mode couplings between the bending/stretching and each of the seven additional modes, and also the quartic terms that correspond to (combination) transitions that lie close to the fundamental OH stretching vibration.

Using this model, we calculated the IR absorption spectrum. The overall ground state was obtained by propagation of an initially guessed Gaussian wave packet in imaginary time using the MCTDH program package [74]. The grid parameters and the number of single particle functions per mode are compiled in Table 4.4. In addition, only the changes of the dipole moment as consequences of the OH bending and stretching motions are taken into account. The spectrum is calculated by performing a Fourier Transform of the dipole autocorrelation function[1] [67]

$$\begin{aligned} I(\omega) &= \frac{4\pi\omega n_{\mathrm{mol}}}{3\hbar c} \sum_{i=x,y} \mathrm{Re} \int_0^\infty dt\, e^{i(\omega-\omega_0)t-\Gamma t} \times \\ &\quad \langle\Psi_0|(\mu_i(Q_b)+\mu_i(Q_s))e^{-iH_{\mathrm{AFF}}t/\hbar}(\mu_i(Q_b)+\mu_i(Q_s))|\Psi_0\rangle. \quad (4.2) \end{aligned}$$

n_{mol} is the volume density and Γ stands for a phenomenological damping parameter that takes into account the lifetime broadening, which might be caused by an interaction with the solvent, for instance. Although we consider the molecules in the gas phase, the damping parameter was introduced in order to obtain the spec-

[1] For all propagations of SA we employed a variable mean field method using the Adams-Bashforth-Moulton predictor-corrector integrator of 6^{th} order with an error tolerance of 10^{-7} and an initial step size 0.01 fs.

mode	SPF	grid	FFT (points)
ν_3	3	-160/250	32
ν_5	3	-160/160	32
ν_7	3	-135/160	32
ν_{12}	3	-90/100	32
ν_{16}	3	-80/80	32
ν_{27}	3	-60/50	32
ν_{30}	3	-40/50	32
ν_{32}	3	-40/40	32
ν_{37}	3	-20/70	32

Table 4.4: The number of single particle functions, the grid dimension (min(Q_i)/max(Q_i) in units of $a_0\sqrt{(\mathrm{a.m.u.})\,m_e}$) for the substrate modes and the number of grid points.

trum from a finite propagation of the wave function. $\boldsymbol{\mu}$ is the dipole moment of the molecule (we considered only the μ_x and the μ_y component since the molecule is planar and lies in the (x, y) plane (cf. Fig. 4.2), the OH bending and stretching vibrations represent an *in plane motion* and $\mu_z = 0$ for all displacements along ν_b and ν_s) and $\hbar\omega_0$ is the energy of the ground state.

The resulting spectrum is displayed in Fig. 4.6, Panel (A). The peak slightly below $1500\ \mathrm{cm}^{-1}$ corresponds to the OH bending vibration, and the one around $2720\ \mathrm{cm}^{-1}$ to the OH stretching mode. The harmonic values are 1457 and 3156 cm^{-1} respectively, Panel (B). The anharmonic terms are responsible for the pronounced red shift of the stretching vibration, but also for the small peak around $3000\ \mathrm{cm}^{-1}$ which is a combination transition of modes ν_s and ν_3. The position of the OH bending fundamental transition is well reproduced, comparing with the experimental spectrum, Fig. 4.3. However, the question is whether the stretching region is correctly described. Namely, the band that corresponds to the OH stretching transition is in the experimental spectrum rather broad, as is usually the case with the bands that correspond to this type of motion, [6]. The question is whether the anharmonicity is fully captured with the AFF method, i.e., whether the two lowest anharmonic terms are sufficient for a reasonable description of the

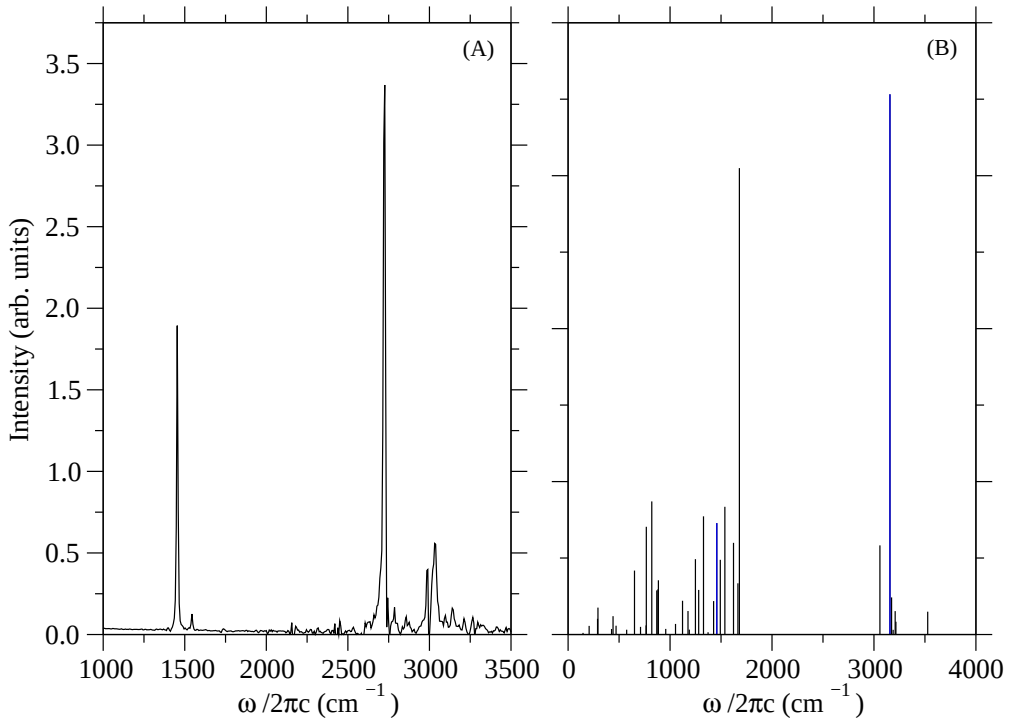

Figure 4.6: (A) IR spectrum for the AFF model of SA. The spectrum was obtained from a 3 ps propagation, with the damping parameter $\Gamma^{-1} = 1.5$ ps. (B) Stick spectrum of SA from the normal mode analysis. The low intensity blue peak stands for the OH bending and the high intensity blue peak for the OH stretching vibration.

PES. That could be checked, in principle, by including higher order anharmonic terms (quintic, etc.). However, the size of the molecule, as well as the number of selected modes indicate that this would require high computational effort. In order to test the quality of the proposed model, we turn to a more general approach, the Cartesian Reaction Surface method introduced in Section 2.2.2, which will be described in the following section.

4.3 The CRS Hamiltonian - Paving the Way to Chemical Reactions

In the previous section, vibrational motion close to the global minimum of the PES was investigated using the Anharmonic Force Field approach. The results presented in this section were obtained with the Cartesian Reaction Surface method (Section 2.2.2). Besides its advantage that the anharmonicity of the hydrogen motion is more rigorously treated, the CRS method can be used for describing processes that also include the *keto* well.

As already mentioned, the optimized structures of the two tautomers are planar, Fig. 4.2. The energetics of the stationary points is shown on Fig. 4.7 and is also

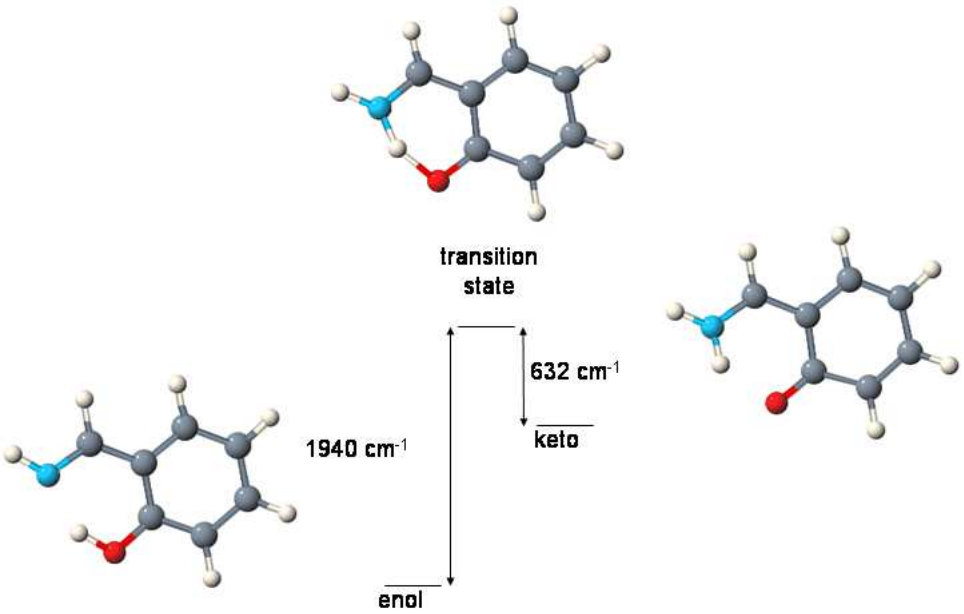

Figure 4.7: The stationary points of Salicylaldimine optimized with the B3LYP exchange-correlation functional and 6-31+G(d,p) basis set: the enol tautomer (left), the transition state (middle) and the keto tautomer (right).

given in Table 4.5. The more stable structure, enol form, is chosen as a reference configuration for the normal mode transformation. As can be seen from Fig. 4.2, the x and y coordinates of the active hydrogen atom undergo large changes during the hydrogen transfer reaction. Since the structures at the stationary points are planar, we considered the *in plane* motion of the reactive hydrogen only. That is, H_x and H_y coordinates have been chosen as **reactive** in the spirit of the CRS approach, whereas the H_z coordinate is treated as belonging to the substrate. Treatment of the H_z coordinate as reactive would not give qualitatively any new contribution, although it would drastically increase the computational effort due to the fact that the Hessian on a three dimensional grid would have to be computed.

	enol	**TS**	**keto**
ΔE_{SPE} (cm^{-1})	0.0	1940	1308
$\Delta E_{\mathrm{reorg}}$ (cm^{-1})	0.0	3573	3112
ZPE (cm^{-1})	27970	27028	27851
$R_{\mathrm{O-H}}$ ($\dot{A}$)	0.999	1.293	1.729
$R_{\mathrm{N-H}}$ ($\dot{A}$)	1.716	1.194	1.038
$R_{\mathrm{O-N}}$ ($\dot{A}$)	2.611	2.406	2.579
d_x (Debye)	0.032	-1.042	-1.743
d_y (Debye)	2.847	3.522	3.842

Table 4.5: Parameters for the stationary points of SA. The single point energies are given with respect to the enol tautomer. The reorganization energy includes all modes, Eq. 2.67. The separation of the hydrogen and the oxygen atom results in an increase of the dipole moment. The Zero point energy (ZPE) was taken from the harmonic analysis.

Large values for $\Delta E_{\mathrm{reorg}}$ at the transition state and the keto structure (cf. Table 4.5) confirm strong interaction between the reactive hydrogen atom and the skeleton vibrations. The change in ZPE is probably mostly due to the hydrogen motion. Since ΔZPE is small, it is probably reasonable to assume that this change is captured by the CRS.

After selecting the reaction coordinates, we are left with 40 substrate normal modes. Table 4.5 suggests that hydrogen displacement is accompanied by skeleton motion, since the $\mathrm{O}-\mathrm{N}$ distance changes along the reaction path. However, all 40 substrate modes cannot be included in the investigation of the dynamics and hence it is necessary to identify those degrees of freedom that have significant influence on the hydrogen dynamics. The five modes that couple most strongly to the reactive coordinates have been chosen according to the values of their reorganization energies, Eq. 2.68, at the TS and for the keto tautomer, and they comprise corres-

i	ω_i (cm^{-1})	ΔE_{reorg} (cm^{-1})	
		TS	keto
4	336	1317	3
6	451	771	88
14	861	1100	55
26	1333	114	635
30	1513	263	755

Table 4.6: Harmonic frequencies of the included modes at the enol configuration of SA, and reorganization energies for each mode at the TS/keto configuration calculated according to Eq. 2.68.

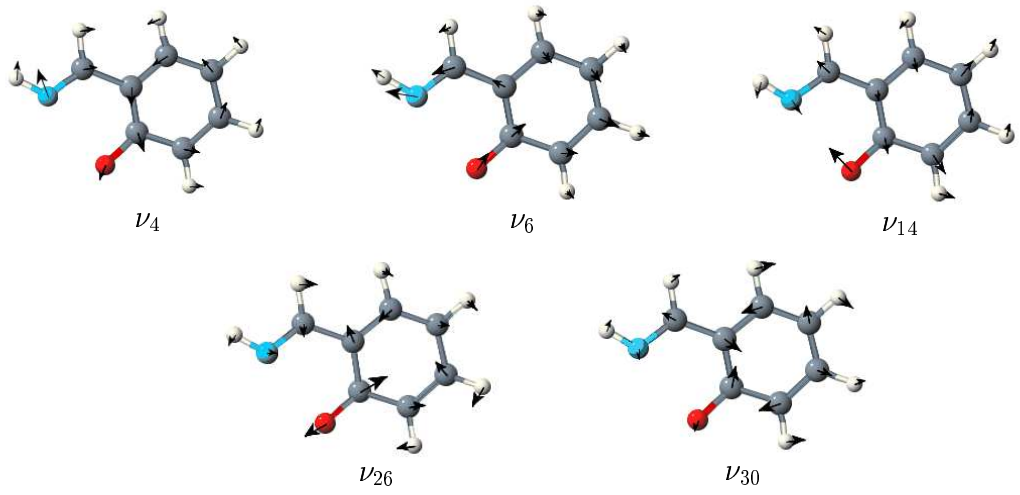

Figure 4.8: Normal mode displacement vectors at the enol configuration for the 5 most important in-plane substrate modes.

pondingly 80% and 46% respectively of the total reorganization energy at these points, Table 4.6. The normal mode displacements are given in Fig. 4.8. Modes ν_4 and ν_{14} are referred to as *promoting modes*, since they mainly involve displacements of the proton acceptor and proton donor respectively, thereby decreasing the distance between them which promotes the hydrogen transfer. Note that those two modes have high reorganization energy at the transition state, where the distance between the oxygen and the hydrogen atom is the shortest. This means that they undergo significant changes upon hydrogen motion from the global minimum of the PES towards the barrier which separates the enol from the keto species. On the other hand, modes ν_6, ν_{26} and ν_{30} are involved in the rearrangement of single

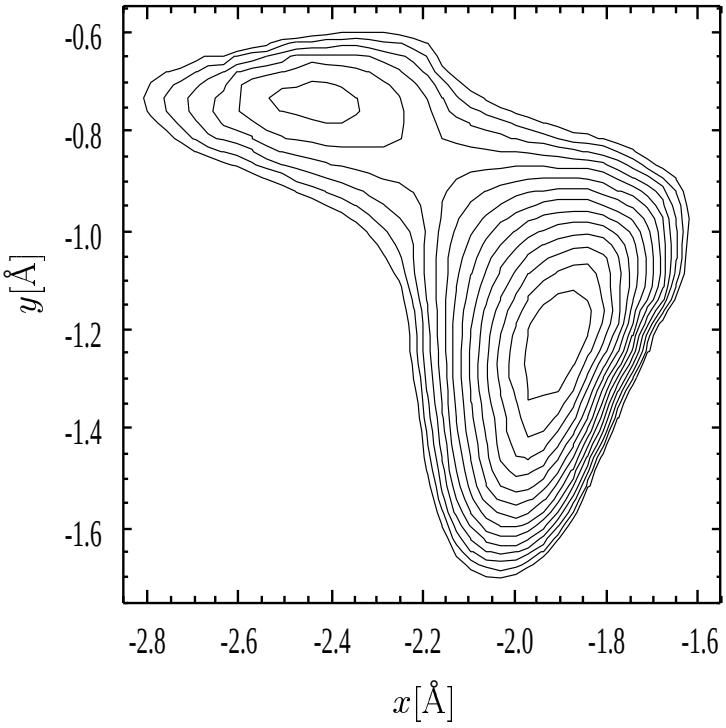

Figure 4.9: Potential energy surface for the reactive coordinates on a 64×64 grid in the interval (in Å) $x \in [-3.3 : -1.3]$ and $y \in [-2.0 : -0.3]$. The contours are given in steps of 500 cm^{-1} up to 6500 cm^{-1}.

and double bonds that accompanies the tautomerization reaction and are, therefore, denoted as *linear coupling modes* [67]. Those five harmonic degrees of freedom together with the two reaction coordinates compose a seven dimensional model for SA.

Although the coordinates of other atoms do not change appreciably, the slight difference of the skeleton among the enol and the keto structure, the energy gap between them, as well as the reorganization energy for the keto tautomer and the transition state (cf. Table 4.5), suggest utilization of a flexible reference (Section 2.2.2) in order to obtain the potential for the reactive coordinates. After optimizing the stationary points, the points along the *linear path*, Fig. 2.4, were obtained as explained in Section 2.2.2. In order to obtain the whole PES, the substrate coordinates were frozen at their equilibrium positions, while displacing the molecule along the reaction coordinates. This 2D potential obtained from 205 points scattered over the reaction valley, Eq. 2.63, is shown in Fig. 4.9. The data were fitted on a regular (64×64) grid employing a bivariate, locally quintic interpolant. The right valley (global minimum) corresponds to the enol tautomer, whereas the left (local) minimum stands for the keto species.

We are now able to calculate the eigenstates corresponding to the *system Hamiltonian*, i.e., the Hamiltonian that involves only the reactive degrees of free-

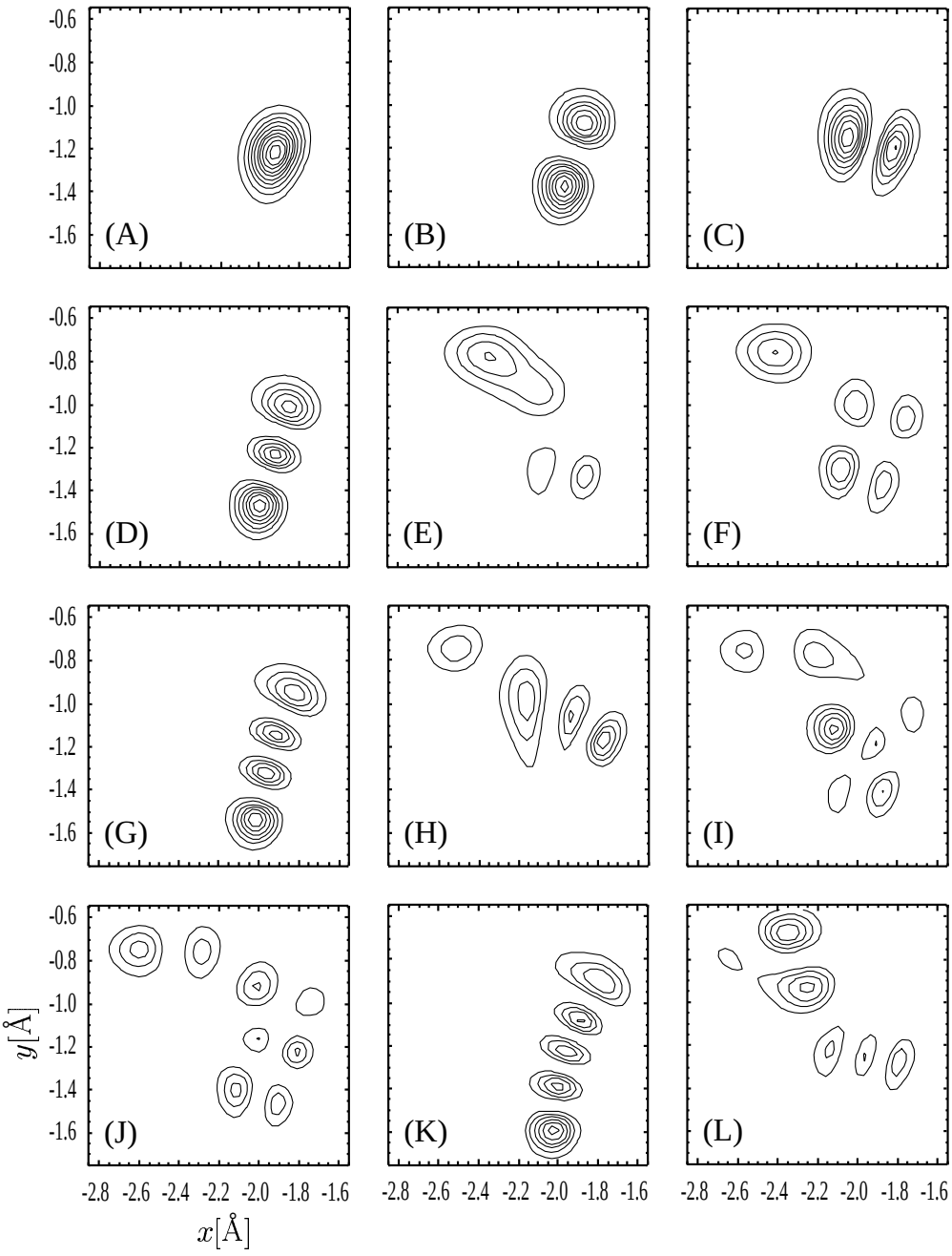

Figure 4.10: Probability densities for the system Hamiltonian. The twelve lowest eigenstates are displayed on Panels (A) - (L).

dom, Eq. 2.78 (the calculations have been performed with the WavePacket program [107]). The four lowest lying states are localized in the enol well, Fig. 4.10. The ground state is displayed in Panel (A). The first excited state, (B), corresponds to the OH bending vibration (ν_b), the second excited state, (C), represents the OH stretching vibration (ν_s), whereas the third excited state, (D), stands for the bending overtone. The fourth excited state, (E), is mainly located in the keto valley. By climbing the PES further, one finds the states lying above the barrier and are delo-

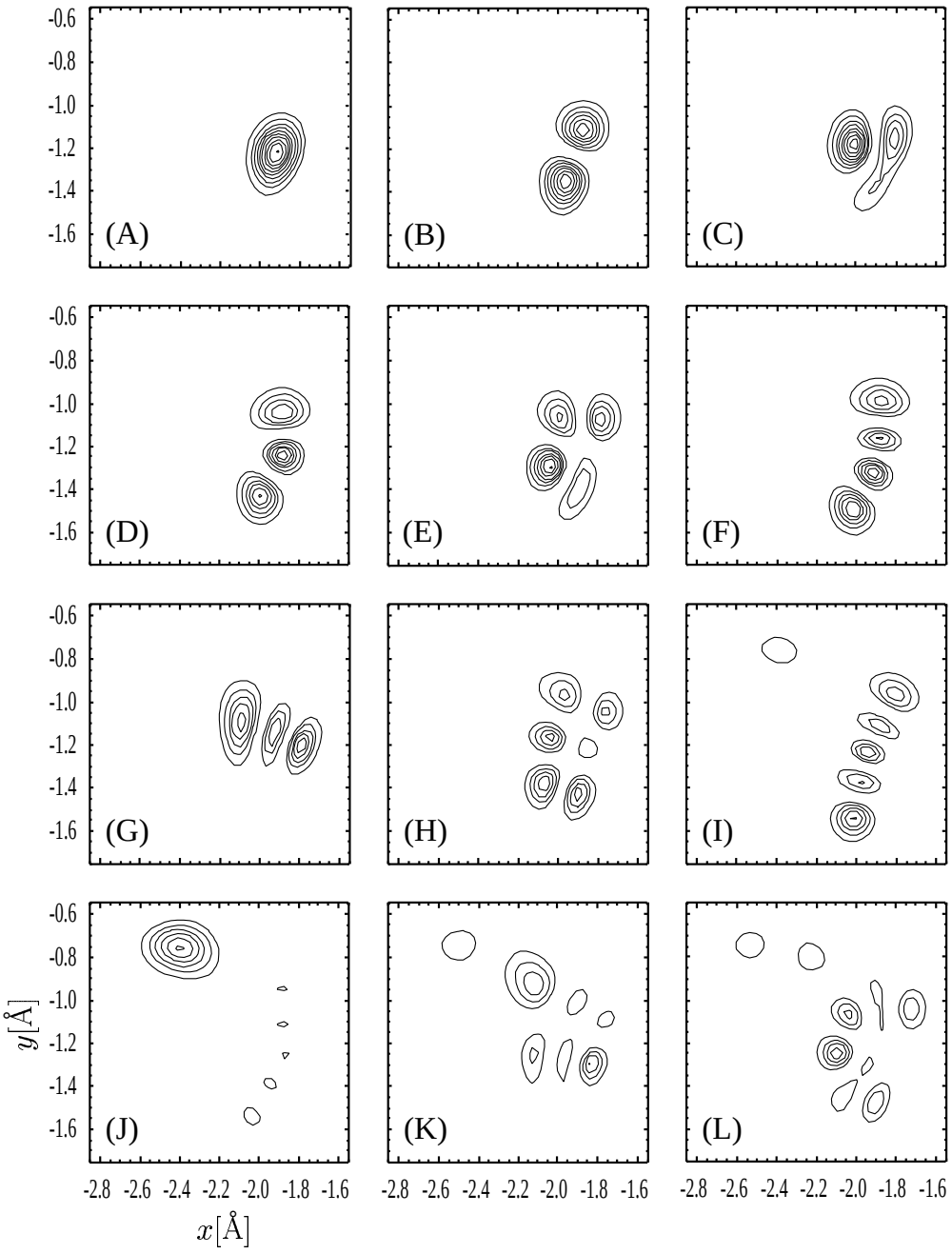

Figure 4.11: Probability densities for the system Hamiltonian of SA-D, corresponding to the lowest eigenstates.

calized over both valleys. For instance, the ninth excited state, as shown in Panel (J). These eigenstates can be considered as reasonable zero order states.

We now turn to investigation of the deuterated molecule. The advantage of the CRS method concerning isotope replacement is that it facilitates straightforwardly an isotope investigation, since the CRS Hamiltonian is mass independent, whereas the AFF method requires recalculation of the quantum chemistry data. Upon deuteration, the vibrational levels shift downwards as a consequence of the higher

SA-H	
level	E (cm^{-1})
1	0
2	1415
3	2611
4	2810
5	3805
6	4062
7	4252
8	4701
9	5139
10	5449
11	5715
12	6096
13	6204
14	6585
15	6835

SA-D	
level	E (cm^{-1})
1	0
2	1013
3	1941
4	2006
5	2938
6	3008
7	3654
8	3894
9	4030
10	4054
11	4534
12	4811
13	4905
14	5069
15	5168

Table 4.7: Energies of the eigenstates of the system Hamiltonian for the protonated (left) and the deuterated (right) SA.

mass of the deuterium comparing to the hydrogen atom (cf. Table 4.7). The corresponding eigenstates of the deuterated Salicylaldimine (SA-D) are depicted in Fig. 4.11. In the previous case (protonated species, SA-H), the first two excited states corresponded to the pure OH bending and stretching vibrations. However, smaller spacing between the energy levels in SA-D leads to stronger mixing between the states. As a result, the 2^{nd} excited state with dominantly OH stretching character has a strong admixture from the bending state, Panel (C). This indicates stronger couplings between the states, which might influence the deuterium dynamics, as compared to the proton dynamics. Higher excited states located in the enol valley represent the overtones and the combination transitions of the OD bending and stretching fundamental vibrations ((D) - (I)). The 9^{th} excited state has dominantly keto character. Note that the keto state of SA-D is stronger localized in the keto well comparing to the protonated species due to the larger mass.

The frequency shifts upon deuteration are often examined in terms of the so-called "$\sqrt{2}$ rule". Consider a harmonic oscillator. Its frequency is given by

$$\nu = \frac{1}{2\pi}\sqrt{\frac{k}{\mu}} \tag{4.3}$$

with k being the force constant and μ the reduced mass of the oscillator (for a normal mode vibration that involves hydrogen motion with respect to a heavy skeleton it is close to the mass of the hydrogen atom). The force constant depends solely on the electrostatic interactions, so it is the same for H and D. Therefore,

$$\frac{\nu_H}{\nu_D} = \sqrt{\frac{\mu_D}{\mu_H}} \approx \sqrt{2}. \tag{4.4}$$

$v(\nu_b)$	$\hbar\omega_H/\sqrt{2}$ (cm^{-1})	$\hbar\omega_D$ (cm^{-1})
$v(\nu_b)$ = 1	1001	1013
$v(\nu_b)$ = 2	1987	2006
$v(\nu_b)$ = 3	3007	3008
$v(\nu_s)$ = 1	1846	1941

Table 4.8: Transition energies that correspond to excitation of the OH bending fundamental and its overtones, starting from the ground state, as well as the OH stretching fundamental transition.

Table 4.8 shows that this rule can be applied to bands that have exclusively bending character, which means that the anharmonicity along ν_b is not pronounced. However, even for the fundamental transition of ν_s, the deviation from the $\sqrt{2}$ rule amounts to 100 cm^{-1}. This is a consequence of the coupling of the OH stretching vibration to other degrees of freedom.

We proceed by taking the matrix elements of the forces and the Hessian with the eigenstates, which leads us to the diabatic representation of the CRS Hamiltonian, Eq. 2.79. Although an overall picture can only be obtained by considering all included normal modes, it is illustrative to focus on a single mode. One dimensional potential energy curves for mode ν_{14}, as defined by Eq. 2.80, are given in Fig. 4.12 for SA-H (left) and SA-D (right). The blue curves correspond to the enol and the keto tautomer. The curves related to the states bounded in the enol valley are centered around $Q_{14} = 0$. However, the curves that are correlated to the keto tautomer undergo the greatest shifts, due to the forces acting on this mode, trying to push the structure along it and drive the molecule to a relaxed configuration (see section 2.2.4). For SA-H, the keto state is energetically well separated from the neighboring states. However, in SA-D it lies close to the adjacent states. The force acting on mode ν_{14} is responsible for a downward shift of the keto curve, causing crossings with the lower states. The figure foretells possible couplings between this state and the three lower lying states (recall the progression with respect to the skeleton normal mode within each diabatic curve, like in Fig. 1.1). It is interesting to note that the other curves that undergo slight shifts have stretching character.

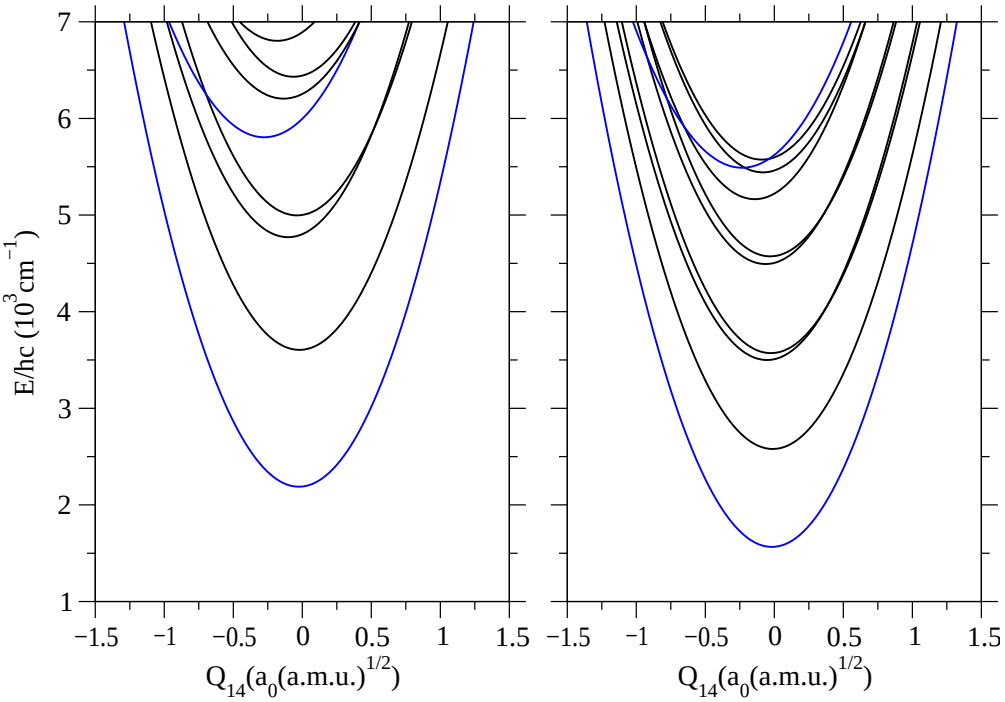

Figure 4.12: Diabatic potential energy curves corresponding to mode ν_{14} for SA-H (left) and SA-D (right). The finite value of the ground state energies is due to the ZPE with respect to the reaction coordinates.

In addition, the sign of the shift is the same as for the keto line. Hence, thinking of a vertical transition, the overlap of the eigenfunctions with the stretching character and the keto eigenfunction might be large, as is the coupling. This suggests possible pathways for the relaxation processes after an excitation of the molecule.

4.4 IR Absorption Spectra for SA-H and SA-D

Having settled the Hamiltonian, we are able to calculate the linear IR absorption spectrum. For the wave packet propagation, we employed the multi-set formalism of the MCTDH approach, Section 2.3.1. The grid parameters, as well as the number of single particle functions per mode are given in Table 4.9. We have included ten diabatic states. The initial state $|\Psi_0\rangle$ is chosen to be the ground state of the 7D model, obtained by a relaxation in imaginary time [73]. The IR spectrum is calculated from the Fourier Transform of the dipole autocorrelation function, Eq. 4.2.

The linear spectrum for the protonated SA is given in Fig. 4.13 (contributions from the y and the x component of the dipole moment are displayed with the blue and the black curve respectively). According to the wave functions of the excited states, Fig. 4.10, the OH bending motion takes place mainly along the y-

axis, whereas the stretching of the OH bond occurs almost parallel to the x-axis. Thus, the excitation of the bending vibration is mainly achieved with μ_y, while the μ_x component turns out to be responsible for the stretching vibration. The high intensity peak around $1400\ \mathrm{cm}^{-1}$ represents the OH bending vibration, and the

	diabatic state (α)											FFT
mode	1	2	3	4	5	6	7	8	9	10	grid	(points)
ν_4	5	4	4	4	4	3	3	3	2	2	-170/170	32
ν_6	5	4	4	4	4	3	3	3	2	2	-130/130	32
ν_{14}	5	4	4	4	4	3	3	3	2	2	-70/70	32
ν_{26}	4	3	3	3	3	3	3	3	2	2	-45/45	32
ν_{30}	4	3	3	3	3	3	3	3	2	2	-40/40	32

Table 4.9: The number of single particle functions per diabatic state, $|\alpha\rangle$, the grid dimension (min(Q_i)/max(Q_i) in units of $a_0\sqrt{(\mathrm{a.m.u.})\,m_e}$) for the substrate modes and the number of grid points.

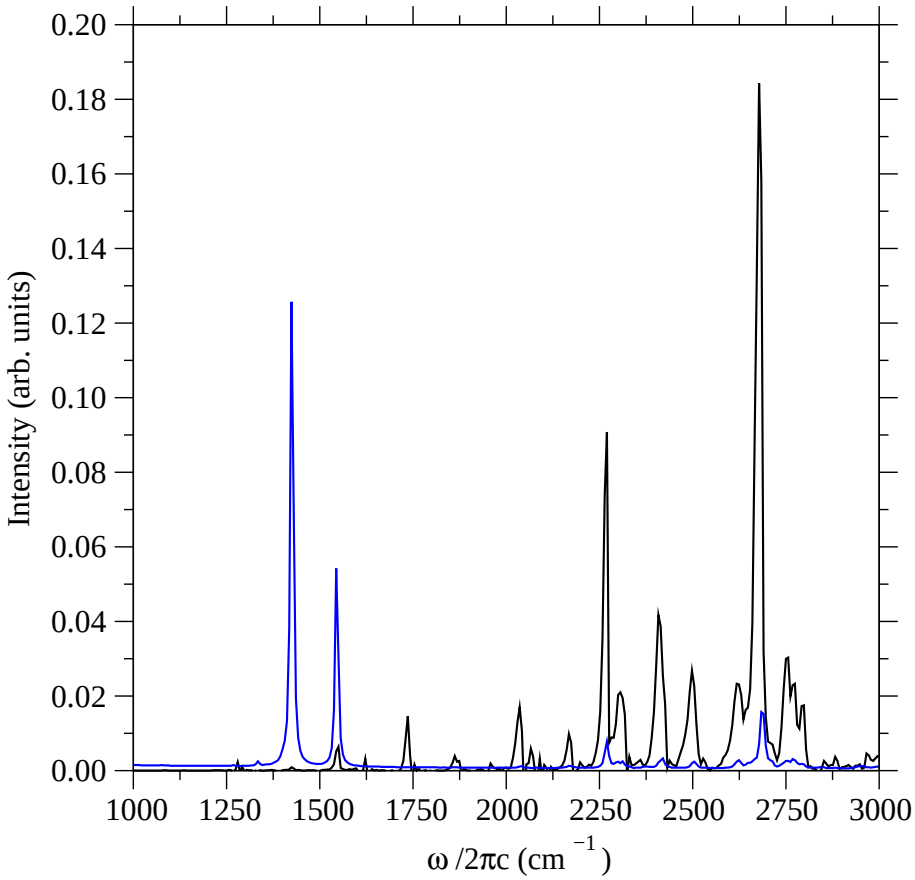

Figure 4.13: Linear absorption spectrum, Eq. 4.2, from a 3 ps propagation. The blue/black line is obtained using the μ_y/μ_x component of the dipole moment. The damping parameter is in both cases $\Gamma^{-1} = 1.5$ ps.

neighboring peak around $1500\ \mathrm{cm}^{-1}$ corresponds to the highest frequency mode, ν_{30}. Contrary to the OH bending region which is narrow, the OH stretching band covers the range between 2200 and $2800\ \mathrm{cm}^{-1}$. The broadness of the stretching region is a consequence of the anharmonicity of the PES, which allows occurrence of overtone and combination transitions, thereby leading to a broad band. In addition to the broadening, the stretching band undergoes a red shift with respect to the harmonic approximation (cf. Fig. 4.6, Panel (B)). This was to be expected, since the shape of the OH stretching band represents a fingerprint for the existence of a hydrogen bond ([4], [6]). The obvious difference in the shape of the bending and the stretching band is an indication of a specific coupling pattern being effective for the corresponding modes.

Concerning the deuterated SA, the anharmonicity of the PES is reflected again in the red shift of the OD stretching vibration, Fig. 4.14, comparing to the harmonic value (which is 1044 cm^{-1} and 2306 cm^{-1} for ν_b and ν_s, respectively). Again, we separate the contributions from the different components of the dipole moment. The excitation of the OD bending vibration occurs around $1100\ \mathrm{cm}^{-1}$,

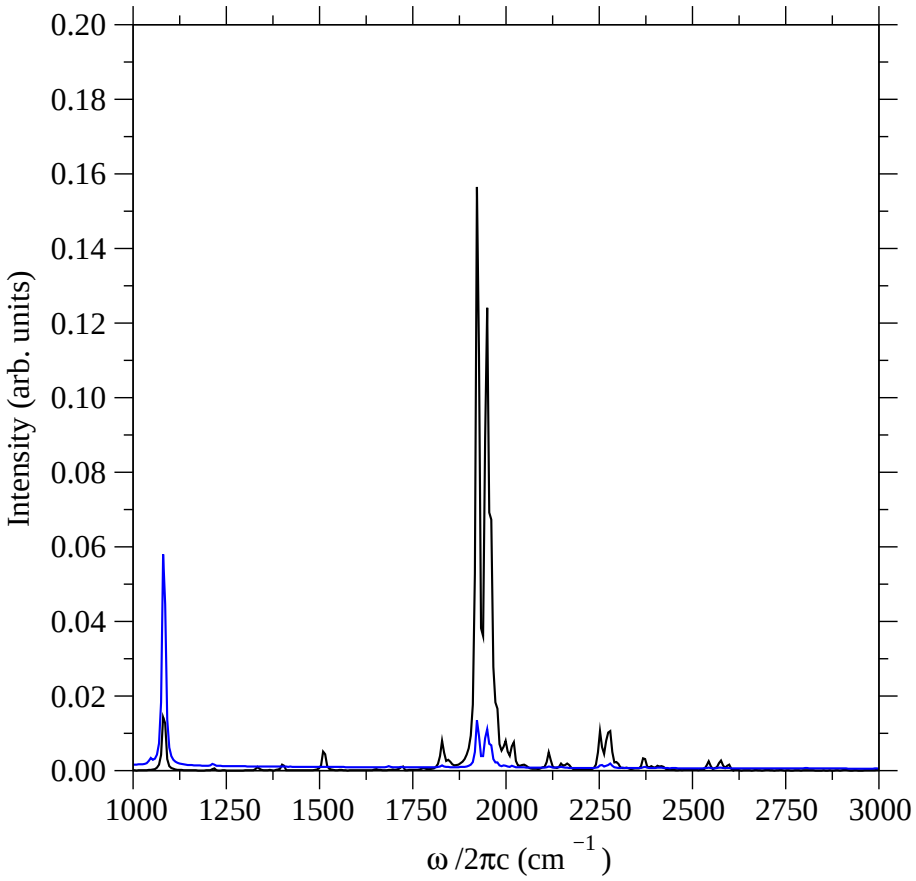

Figure 4.14: Linear spectrum for SA-D (3 ps propagation). The blue and the black line correspond to the cases where the μ_y and the μ_x component of the dipole moment have been used respectively ($\Gamma^{-1} = 1.5$ ps).

while the OD stretching region lies slightly below $2000\ \mathrm{cm}^{-1}$. Note also the red shift with respect to the SA-H bands. However, the stretching region is much narrower and less structured than the one of the protonated species. It is marked by the existence of two peaks, one of them being attributed to the fundamental OD stretching transition, and the other to the OD bending overtone. That is, the particular shape of the spectrum is a consequence of the Fermi resonance.

Another interesting feature is the disappearance of the double peak structure in the region $1400 - 1500\ \mathrm{cm}^{-1}$. For SA-H the peak corresponding to ν_{30} had high intensity due to the coupling to the OH bending vibration, which lead to the borrowing of the oscillator strength [51]. Upon deuteration, the red shift of the bending vibration (with respect to the protonated molecule) leads to a large separation between the two peaks, disabling the interaction between the corresponding modes.

Additionally, the correspondence between the experimental and the computed positions of the OH/OD bending and stretching regions suggest that the phenol group does not have an important influence on the motion of the hydrogen atom. Further, the loss of the double peak structure encountered through deuteration implies that similar types of motion of the SA-H and SA-Ph scaffolds couple to the hydrogen atom.

Comparing the results obtained with the AFF method, Fig. 4.6, and with the CRS technique, Fig. 4.13, the agreement with the positions of the ν_b and ν_s bands is good. However, the flat region between the two peaks in the former spectrum is an indication that the anharmonicity has not been correctly treated with the AFF method. That is, the two lowest anharmonic terms were not sufficient to describe properly the couplings between the normal modes in this rather anharmonic double minimum system.

Convergence of Results Obtained Using the Single-set and the Multi-set Formalism

The linear IR spectrum for SA-H (using the μ_x component of the dipole moment) was also obtained by employing the single-set formulation for the purpose to compare the effort of the two formulations. Fig. 4.15 shows the two spectra which are essentially identical. In order to keep the maximum natural orbital population of the single particle function giving the smallest contribution below 8×10^{-5}, we used 7, 7, 6, 4, and 4 single particle functions for modes ν_4, ν_6, ν_{14}, ν_{26}, and ν_{30}, respectively, which amounts to $47\ 040$ configurations in the MCTDH scheme. The number of configurations within the multi-set formalism (cf. Table 4.9) was $484\ 704$. The propagation up to 3 ps was performed on HP RX2600 (running on

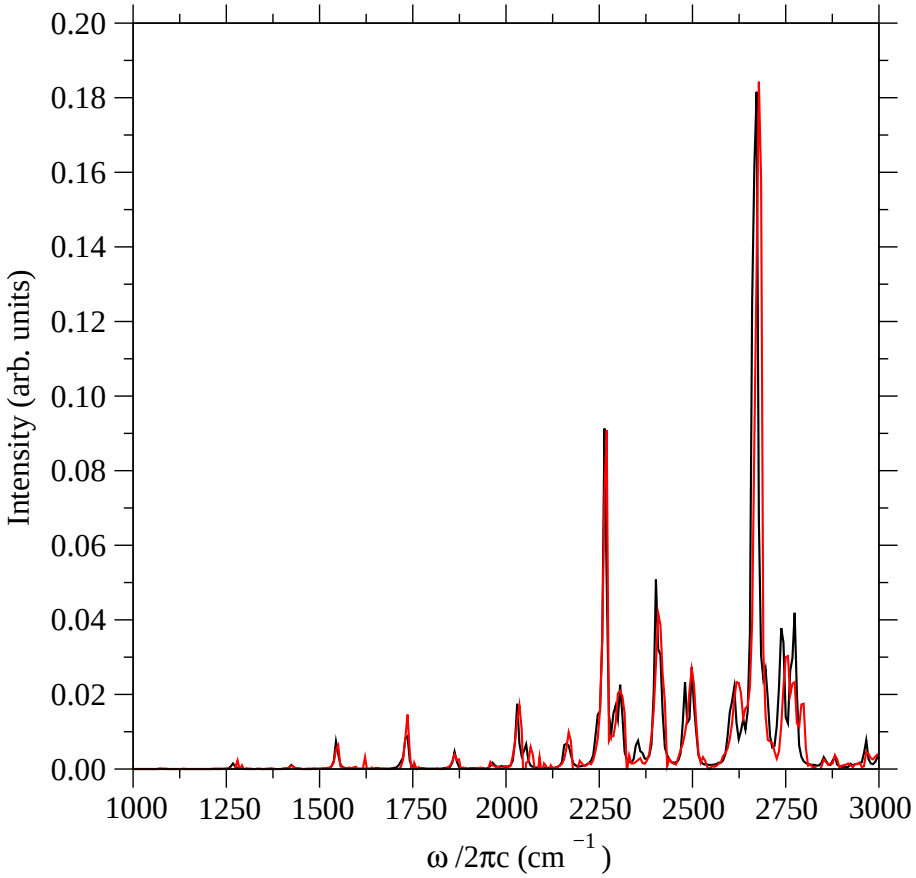

Figure 4.15: Absorption spectra for SA-H from 3 ps propagations using the μ_x component of the dipole moment ($\Gamma_x^{-1} = 1.5$ ps). The red and the grey line stand for the calculations with the multi and the single-set respectively.

HP-UX with two 1.3 GHz Itanium2) using 9.0 MB of memory within $92\ 689.46$ s with the single and with 6.1 MB during $81\ 357.88$ s with the multi-packet formalism. Those results show that the later method is preferable for this system, since it requires smaller computational effort.

The IR spectra of our model system give an insight into the properties of the PES, as well as possible couplings between different degrees of freedom. Attempts to assign the spectrum would be difficult and probably meaningless, especially in the region of ν_s. More information can be obtained by studying the dynamics of the system. In this and the following sections the dynamics of the OH/OD bond will be considered.

4.5 Ultrafast IR Laser Driven Dynamics

4.5.1 Excitation of the OH/OD Bending Motion

We start the discussion of the dynamics in SA by considering the bending vibration of the OH(D) bond, i.e., $|\alpha = 2\rangle$ diabatic state. Were this mode not coupled to the skeleton modes, its excitation would be characterized by energy increase of the hydrogen atom and the skeleton motion would not be affected. However, due to the presence of the hydrogen bond, it is to be expected that hydrogen motion would influence the dynamics of the skeleton atoms.

OH Bending Mode

Let us focus first on the dynamics of the system after an excitation of the OH bending vibration. We used a sin^2 pulse as described in Section 2.3.3. The duration of the pulse is τ = 260 fs, the amplitude $\varepsilon_0 = 4 \times 10^{-3}\ E_h/ea_B$ and the carrier frequency is tuned in resonance with the bending mode, $\Omega = 1425\ \mathrm{cm}^{-1}$, as obtained from the IR spectrum, Fig. 4.13. Since the bending motion takes place dominantly along the y axis, the applied field is taken to be oriented in the same direction, i.e., $\mathbf{e} = \mathbf{e}_y$.

After the pulse had been switched off, we followed the field free propagation of the wave packet. The total propagation lasted 2 ps. The energy of the reaction coordinates is calculated according to

$$E_{xy}(t) = \sum_{\alpha} E_{\alpha} \langle \Psi(t)|\alpha\rangle\langle\alpha|\Psi(t)\rangle. \tag{4.5}$$

In order to understand the energy flow from the reaction coordinates into the normal modes, we define the energy of the uncoupled modes

$$E_{\nu_i}(t) = \frac{1}{2}\sum_{\alpha\beta}\langle\Psi(t)|\alpha\rangle[P_i^2\delta_{\alpha\beta} - 2\langle\alpha|f_i(x,y)|\beta\rangle Q_i + \langle\alpha|K_{ii}(x,y)|\beta\rangle Q_i^2]\ \langle\beta|\Psi(t)\rangle. \tag{4.6}$$

Uncoupled means that the interaction between the modes, K_{ij}, is neglected, while keeping the coupling between the states (the off-diagonal elements $\langle\alpha|f_i|\beta\rangle$ and $\langle\alpha|K_{ii}|\beta\rangle$ are responsible for a population transfer, due to the interaction between the reactive and the i^{th} harmonic coordinate). Specifically, we aim at describing the modification of hydrogen motion (after an excitation by an external field) which is due to its coupling with the skeleton modes. The mode - mode coupling is included in the Hamiltonian, Eq. 2.79, so the consequences of such interaction will be reflected in the dynamics. The populations of the diabatic states are obtained from

$$P_{\alpha}(t) = \langle\Psi(t)|\alpha\rangle\langle\alpha|\Psi(t)\rangle. \tag{4.7}$$

Energy and population changes are displayed in Fig 4.16. Due to its finite width (160 cm^{-1}), the pulse simultaneously excites both the OH bending vibration and mode ν_{30}, Panel (A). Modes ν_4 and ν_{14} are also slightly excited, whereas the two modes, ν_6 and ν_{26} show a negligible energy change. Population changes of the diabatic states, depicted in Panel (B), evince that mainly the two lowest states take part in the dynamics. The depopulation of the ground state is accompanied by population of the first excited state. The slow oscillations of $E_{xy}/E_{\nu_{30}}$ are in phase with

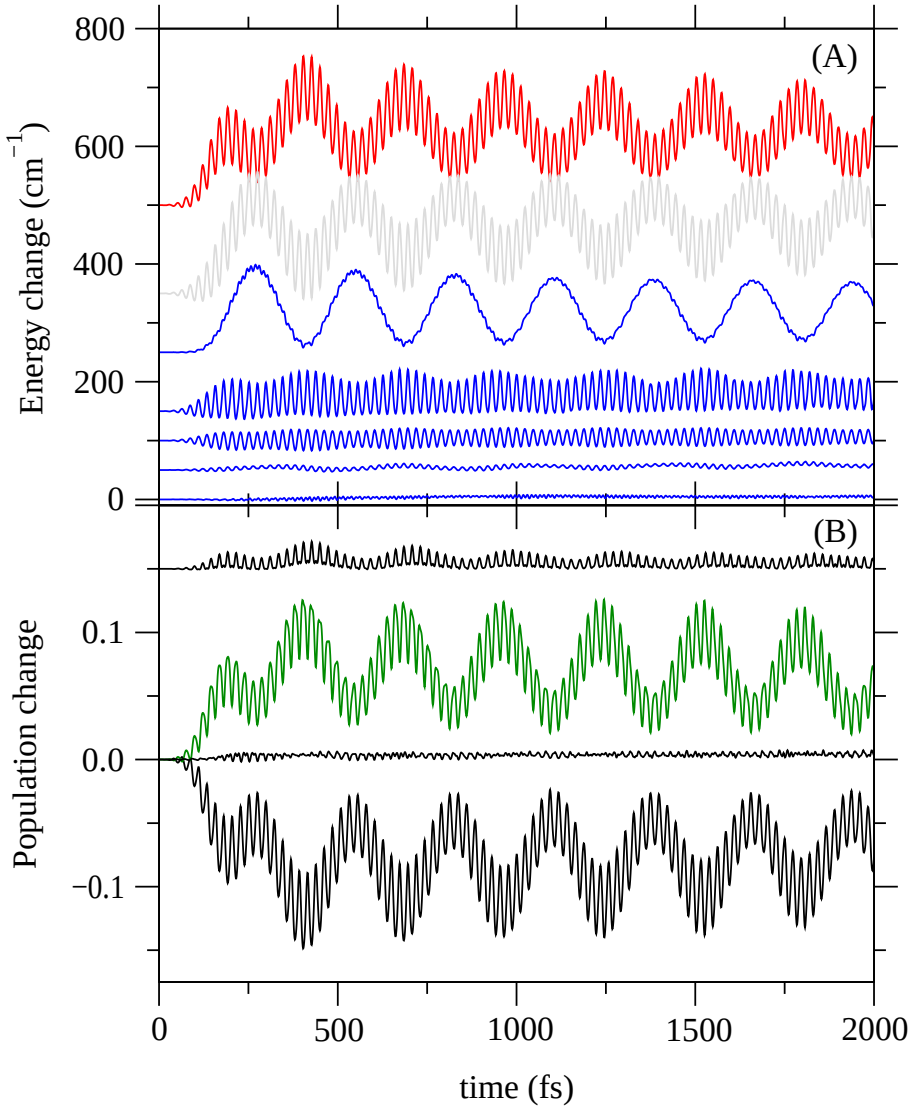

Figure 4.16: (A) Energy change with respect to time zero for the two reaction coordinates, E_{xy} (red line), $\sum_i E_{\nu_i}$ (grey line) and the five uncoupled normal modes, $E_{\nu_{30}}$, $E_{\nu_{14}}$, E_{ν_4}, $E_{\nu_{26}}$, E_{ν_6} (blue lines, from top, the curves are vertically offset). (B) Population change of the diabatic states with respect to time zero: ΔP_1, $\sum_{\alpha=3,5-10} P_\alpha$, P_2 and P_4 (curves from bottom to top, the upper curve vertically offset).

the oscillations of the population of the $|\alpha = 2\rangle/|\alpha = 1\rangle$ diabatic state. That is, the energy exchange mainly takes place between the mode ν_{30} within the ground diabatic level and the bending mode. In addition, the bending overtone $|\alpha = 4\rangle$ is excited either by a two photon process, or via the bending fundamental as an intermediate state. Besides this strong coupling between the hydrogen atom and ν_{30}, the fast oscillations of the energy of the reaction coordinates are due to the interaction with the other skeleton modes, in particular ν_{14}. Also, $E_{\nu_{14}}(t)$ is characterized by slow modulations that follow $E_{xy}(t)$.

A better insight into factors that cause energy changes of the mode ν_{30} can be obtained from Fig. 4.17 which contains separate contributions to the total energy, $E_{\nu_{30}}$ (cf Eq. 4.6). The lowest curve corresponds to the energy change arising from the force acting on this mode. As emphasized before, existence of the force is a consequence of the coupling between the hydrogen atom and the normal mode, and it tries to displace the molecule along this mode. This change of structure in principle may bring the system in a more stable configuration. The change is periodic and the period depends on the strength of the above mentioned coupling. The next curve describes changes in the potential energy originating from

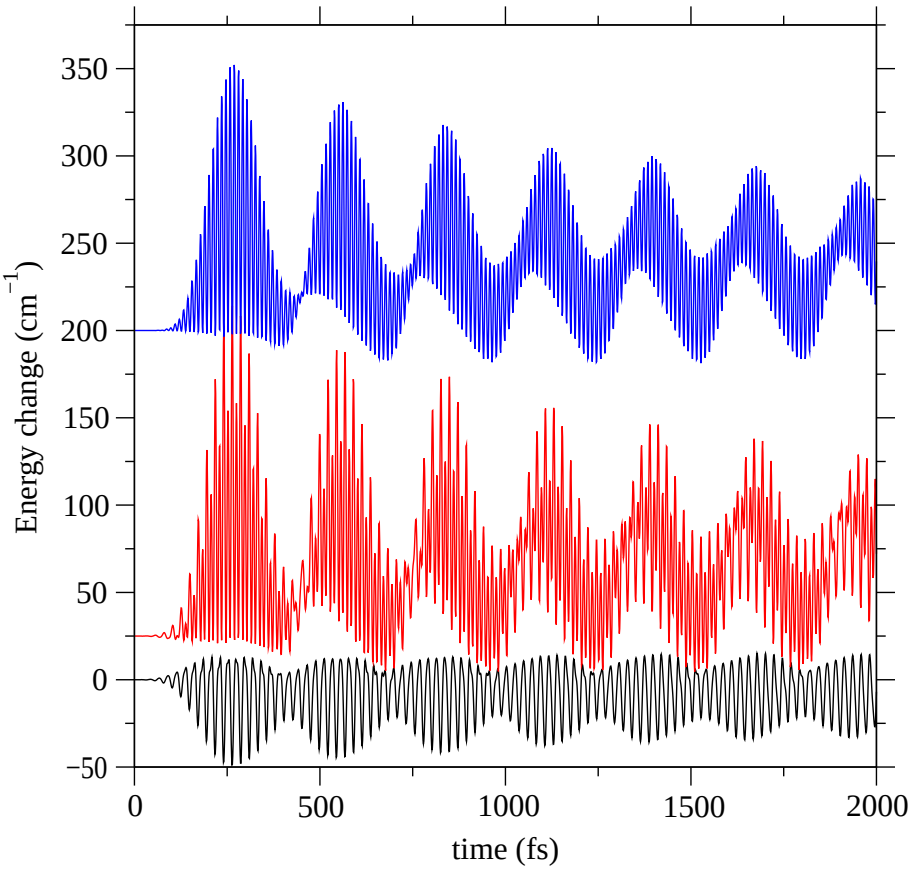

Figure 4.17: Different contributions to the total energy of the mode ν_{30}. From bottom to top: fQ, $1/2KQ^2$, and the kinetic energy T (cf Eq. 4.6).

the change of the normal mode's frequency that accompanies hydrogen motion. These changes are much more pronounced, i.e., the amplitude of oscillations of the $1/2K_{30}Q_{30}^2$ term is higher than the one of the $f_{30}Q_{30}$ term. That is, on the average $\langle f_{30}Q_{30}\rangle \ll \langle 1/2K_{30}Q_{30}^2\rangle$. Finally, the upper curve describes changes in the kinetic energy. Although its initial increase is mainly due to the excitation of mode ν_{30} with the laser pulse, the slow in - phase oscillations with the $1/2K_{30}Q_{30}^2$ term suggest that the changes of the potential energy cause modifications of the kinetic term. Getting a full understanding of this phenomenon is not straightforward due to the complexity of the model. However, since the curves in Fig. 4.17 represent average values over all diabatic states, the model can be simplified by treating it as a single effective normal mode oscillator with a time dependent potential. That is, the force constant can be considered to be time dependent: the increase of the average $\langle 1/2K_{30}Q_{30}^2\rangle$ is a consequence of the increase of K_{30}, which results in a steeper potential. Further, this *contraction* of the potential causes the acceleration of the wave packet, which results in an increase of the average kinetic energy. The fast oscillations of the two higher curves are out of phase, so the sum of all terms results in a relatively smooth curve representing $E_{\nu_{30}}(t)$, Fig. 4.16.

To summarize, the OH bending mode is most strongly coupled to mode ν_{30} and this interaction is responsible for the oscillatory form of $E_{xy}(t)$ and $E_{\nu_{30}}(t)$ which remains until the end of the propagation. Nevertheless, the amplitude of those oscillations gradually decreases with time, owing to the interaction with the remaining modes. An exponential fit of $E_{xy}(t)$ gives an IVR time of about 4.4 ps, which is a rather long period of time on a molecular time scale. This is a consequence of the bending vibration being strongly coupled to a single skeleton mode only.

OD Bending Mode

Since the bending regions in the IR spectra of SA-H and SA-D are considerably different, it is to be expected that the behavior upon excitations of the bending modes of the two systems would be dissimilar. The OD bending vibration was excited by an IR laser pulse with the same parameters as the OH bond in the previous example, except for the carrier frequency which was in this case $\Omega = 1085\ \mathrm{cm}^{-1}$. The energies of the reaction coordinates and the uncoupled modes are displayed in Fig. 4.18, Panel (A). The laser pulse excites mainly the reaction coordinates, but after the pulse had been turned off the energy content of the reactive degrees of freedom started to decrease. This decrease is accompanied by pulsing which characterizes also $E_{\nu_{14}}(t)$. Interaction between the OD bending vibration and ν_{14} is reflected in this characteristic beating, whereas out of phase fast oscillations conform energy exchange among the two modes. Although mode ν_{14} is identified as the one that

couples most strongly to deuterium, increase in the energy content of the other degrees of freedom testifies that the other four skeleton modes also take part in the dynamics, especially ν_4. It is interesting to see that on this time scale (2 ps) during the free propagation the average value of E_{ν_4} stays almost constant, whereas the energies of the other modes gradually increase. That is, ν_{14} is responsible for the beating pattern of E_{xy}, while the relaxation of the deuterium atom is a result of its interaction with the other degrees of freedom. In the previous case, the OH bending mode coupled mainly to ν_{30}. However, this mode has the smallest influence

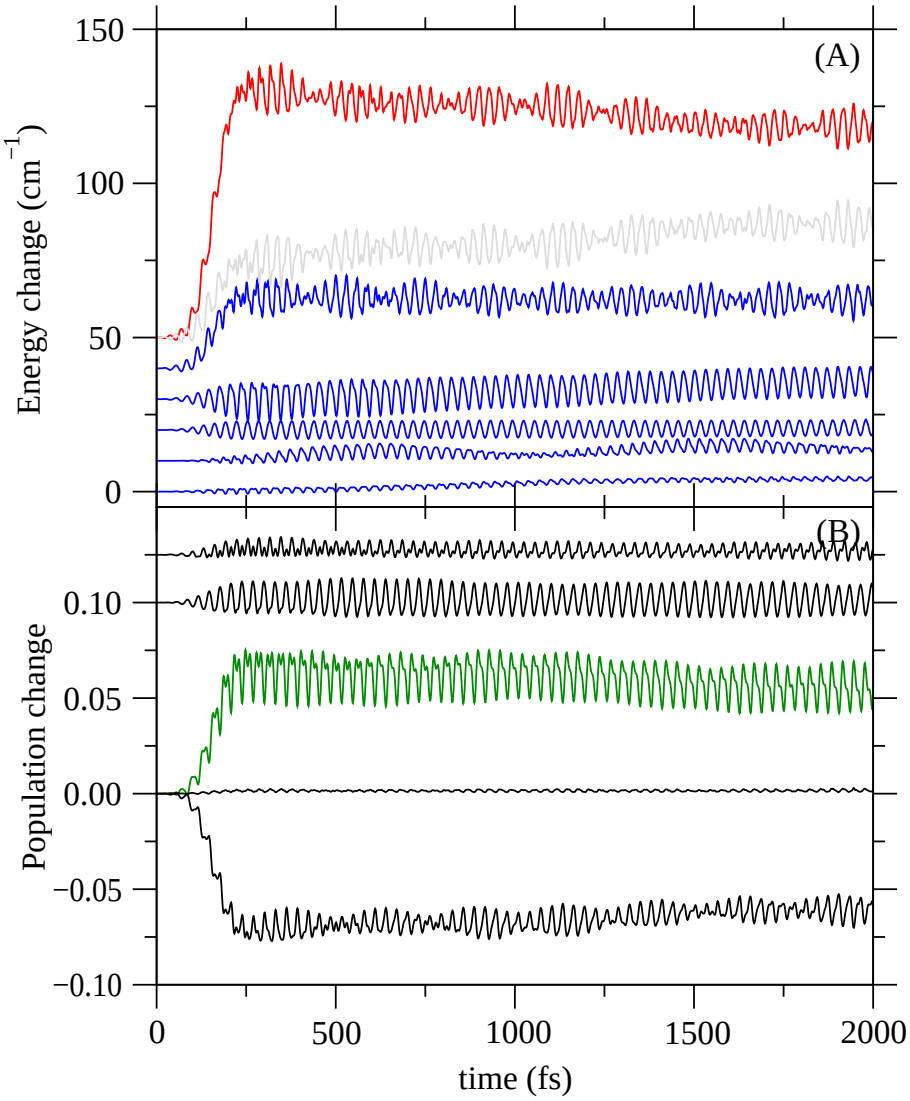

Figure 4.18: (A) Energy change with respect to time zero for the two reaction coordinates, E_{xy} (red line), $\sum_i E_{\nu_i}$ (grey line) and the five uncoupled normal modes, $E_{\nu_{14}}$, E_{ν_4}, $E_{\nu_{26}}$, E_{ν_6}, $E_{\nu_{30}}$ (blue lines, from top, the curves are vertically offset). (B) Population change of the diabatic states with respect to time zero: ΔP_1, $\sum_{\alpha=5-10} P_\alpha$, P_2, P_3 and P_4 (curves from bottom to top, the upper curve vertically offset).

on the bending OD motion due to the large energy mismatch.

The population changes of the diabatic levels are shown on Fig. 4.18, Panel (B). The depopulation of the ground state is accompanied by increase in population of the three lowest excited states. Most of the population flows into the bending level, $|\alpha = 2\rangle$. In addition, the stretching mode $|\alpha = 3\rangle$ and the bending overtone $|\alpha = 4\rangle$ undergo slight excitation. The bending overtone is excited by the same mechanisms as the OH bending overtone (by a two photon transition, or via the bending fundamental). Concerning the stretching mode, it was already noted that this zero - order state does not correspond to the pure OD stretching vibration, but possesses a slight bending character which implies its coupling to the bending fundamental and the bending overtone.

The importance of separate terms which sum up to the total energy of mode ν_{14} are displayed on Fig. 4.19. The potential energy terms show an appreciable change. In this case the importance of the two terms is comparable, i.e., $\langle f_{14}Q_{14}\rangle \approx \langle 1/2K_{14}Q_{14}^2\rangle$. On the other hand, the changes of the kinetic energy term are not as pronounced as for the $1/2K_{14}Q_{14}^2$ term. That means that a simple one - dimensional time dependent harmonic oscillator is not a good approximation

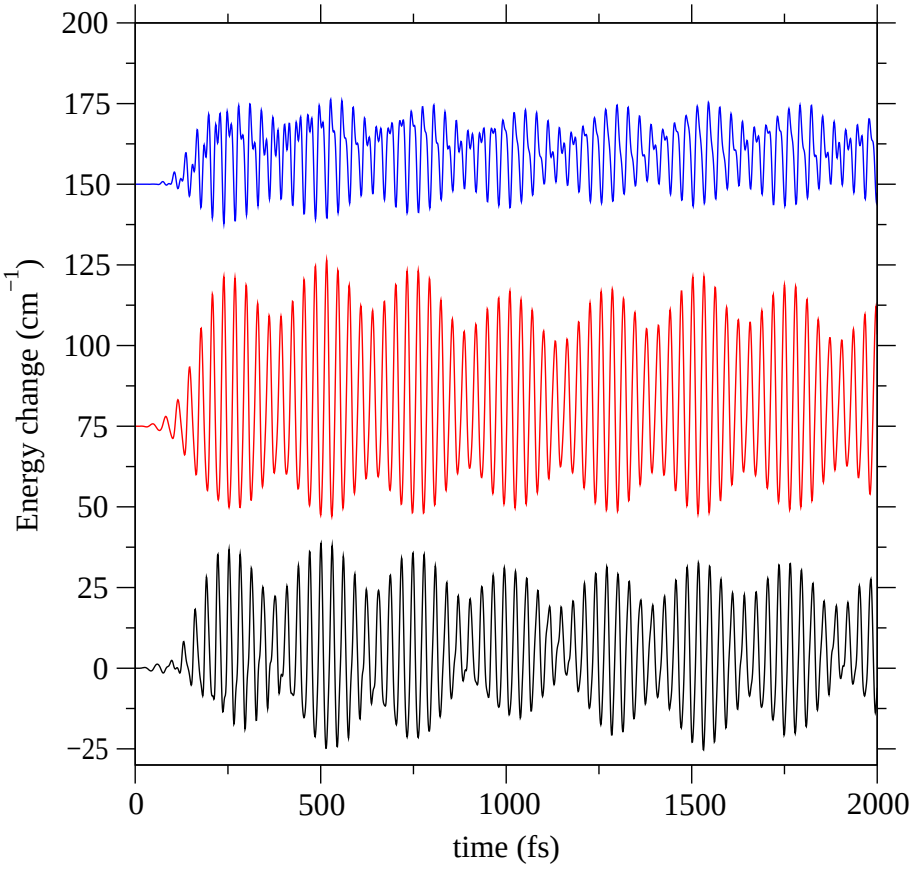

Figure 4.19: Different contributions to the total energy of the mode ν_{14}. From bottom to top: fQ, KQ^2, and the kinetic energy T.

for this system.

Expectation Values of the Reaction Coordinates

Finally, let us compare the expectation values of the x and the y component of H and D, Fig. 4.20

$$\mathrm{H(D)}_r(t) = \langle \Psi(t)|r|\Psi(t)\rangle \tag{4.8}$$

where r can be x or y. In both cases, as expected, the amplitude in the y direction is much larger. $\mathrm{H}_x(t)$ and $\mathrm{H}_y(t)$ are marked with beatings - the increase in amplitude coincides with the increase in energy of the hydrogen atom (cf. Fig. 4.16). Since the hydrogen atom does not leave the enol well and the excitation is not high, the oscillations take place around the equilibrium position. The amplitude shows a slight decrease in time, due to the diminishing of the amplitude of E_{xy}. The deuterium dynamics is not marked by high amplitude energy oscillations, therefore the change of D_x and D_y is not marked by beatings (large amplitudes of E_{xy} for SA-H , Fig. 4.16, can clearly be seen in the position expectation values of the hydrogen atom, whereas small beatings of E_{xy} for SA-D, Fig. 4.18 cannot easily be noticed by expecting the change of the position of the deuterium atom). Comparing the amplitudes of H_y and D_y, the former is slightly higher due to the fact that the energy level of the OH bending vibration lies above the one of the OD bending

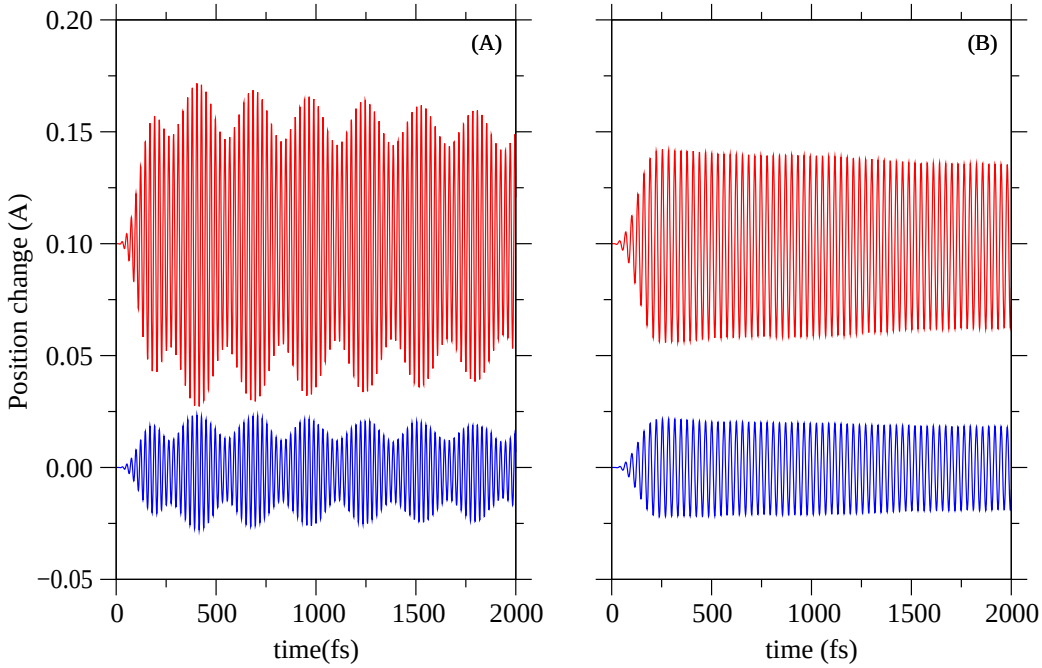

Figure 4.20: Expectation values of the reaction coordinates upon an excitation of the OH (A) and OD (B) bending vibration. In both cases, the blue curve describes the motion in the x, and the red in the y direction.

mode. Furthermore, since the diabatic levels of the deuterated species lie closer to each other and the spacing between them is smaller, the excitation of the 2^{nd} excited state (OD stretching vibration) is reflected in more pronounced motion in the x direction (that is, the relative excitation in the y and the x direction is smaller for SA-D).

4.5.2 Dynamics of the OH/OD Stretching Vibration

After discussing the dynamics of the bending motion, we turn to investigation of the OH and OD stretching vibration, $|\alpha = 3\rangle$. Rich structure of the bands in these regions of the IR spectra indicates a pronounced role of more than one skeleton degree of freedom. Our goal is to understand the dynamics behind the complex IR spectral patterns.

OH Stretching Mode

The OH stretching motion was triggered by sin^2 pulse with the same amplitude and duration as before, ε_0 = 4 $\times$ 10^{-3} E_h/ea_B and $\tau = 260$ fs respectively, the carrier frequency is Ω = 2680 cm^{-1}, and the applied field is oriented along the x axis, i.e., $\mathbf{e} = \mathbf{e}_x$.

Fig. 4.21, Panel (A), shows the dynamics of the energy of the reaction coordinates and the uncoupled normal modes. The reaction coordinates initially accept most of the energy, but the skeleton modes get excited as well. All harmonic modes take part in the dynamics, which means that all of them form the stretching band. This causes very fast internal energy redistribution, with the estimated time for the relaxation of reactive modes of about 0.7 ps. The calculated IVR time is in a relatively good agreement with preliminary experimental results for SA-Ph[106]. It was mentioned that the present model is, according to the IR spectra, a good approximation for the SA-Ph molecule. Moreover, the experiments were performed in solution (CCl_4 was used as a solvent), whereas the calculations correspond to the gas phase. This means that the intramolecular processes in this system take place faster than the intermolecular ones. This is to be contrasted with the less anharmonic system, PMME, studied in Chapter 3. There the interaction with the solvent was vital for the understanding of the fast relaxation dynamics. Another interesting feature is that the decay of E_{xy} is marked by a low frequency modulation with a time scale of about 400 fs. That is to say, although the described dynamics is of considerable complexity, it is possible to observe a modulation of the energy change over three periods.

Concerning the population changes, most of the population from the ground state flows to the stretching level $|\alpha = 3\rangle$, although the bending mode $|\alpha = 2\rangle$ and

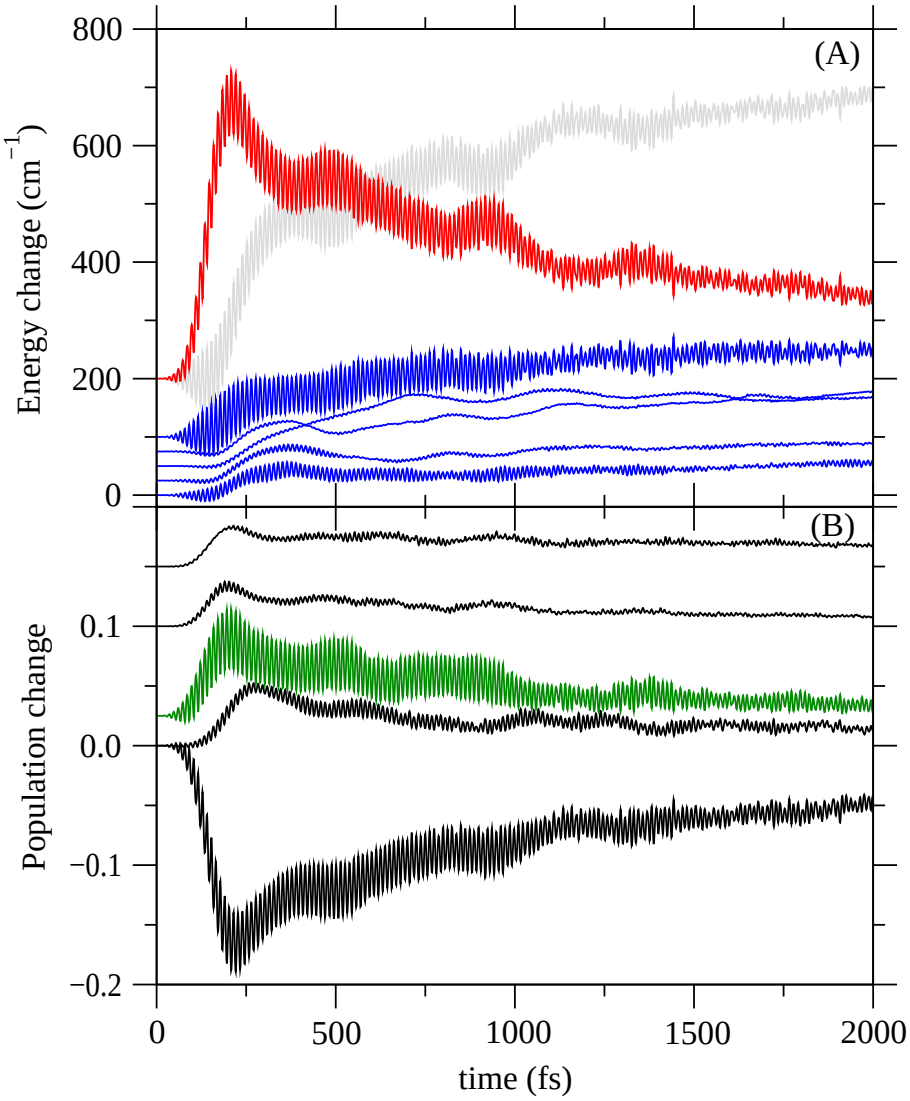

Figure 4.21: (A) Energy change with respect to time zero for the two reaction coordinates, E_{xy} (red line), $\sum_i E_{\nu_i}$ (grey line) and the five uncoupled normal modes, $E_{\nu_{14}}$, $E_{\nu_{30}}$, $E_{\nu_{26}}$, E_{ν_6}, E_{ν_4} (blue lines, from top, the curves are vertically offset). (B) Population change of the diabatic states with respect to time zero: ΔP_1, P_2, P_3, P_5 and $\sum_{\alpha=4,6-10} P_\alpha$, (curves from bottom to top, the upper curves vertically offset). Note that the roughness of the curves is a consequence of the finite resolution.

the bending overtone $|\alpha = 4\rangle$ are also populated (even though to a much lower extent). This is a consequence of the combination of the fundamental bending vibration and normal modes forming a part of the stretching band, and also the bending overtone lying close to the fundamental stretching transition. This can be further clarified by examining Fig. 4.22, where the diabatic potential energy curves of the skeleton degrees of freedom together with the corresponding vibrational levels are displayed. Obviously, in the region of ν_s the density of states with respect to

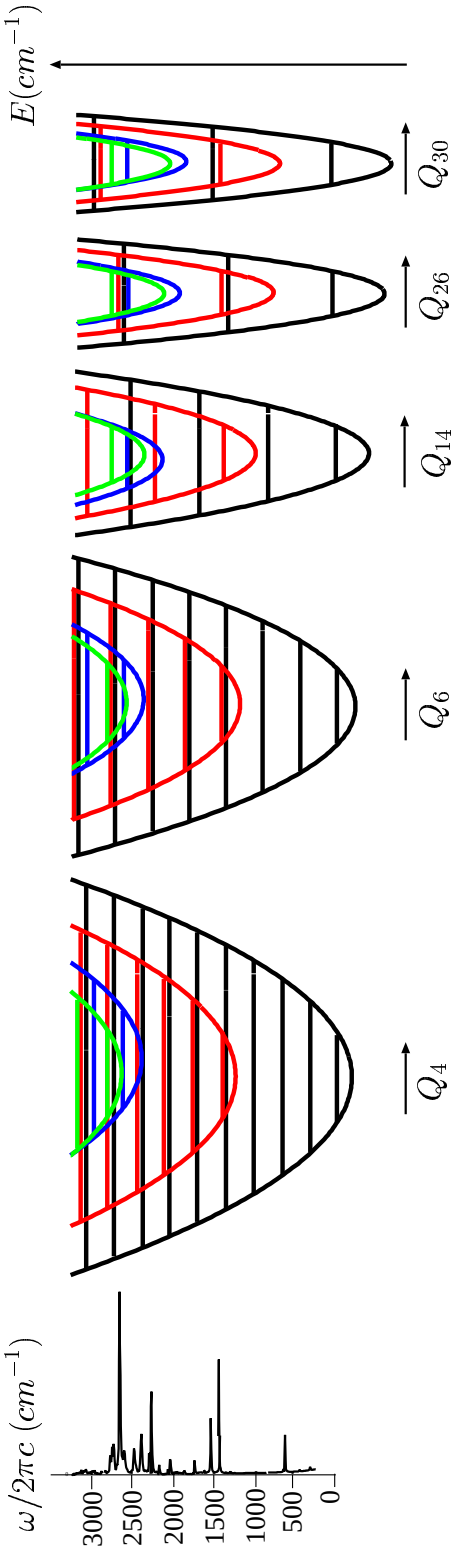

Figure 4.22: 1D potential energy curves are displayed together with the corresponding vibrational levels for modes ν_4, ν_6, ν_{14}, ν_{26} and ν_{30}. The black line corresponds to the ground diabatic level, while the red, blue and green lines stand for the 1^{st}, 2^{nd} and 3^{rd} excited state, respectively. Left: the linear IR spectrum obtained with the total dipole moment from a 3 ps propagation, with Γ^{-1} = 1.5 ps.

each normal mode is rather large. However, one should keep in mind that with this scheme the mode - mode couplings as well as the diabatic state couplings are not considered. In other words, the 7D model is more complex as compared to Fig. 4.22; the energies are shifted and combination transitions contribute to the spectrum.

Concerning higher diabatic levels, the keto state $|\alpha = 5\rangle$ also gets slightly populated, presumably via a two - photon transition. We will return to this point in Section 4.7.

OD Stretching Mode

We turn now to the OD stretching vibration. It was excited with an IR laser pulse characterized by same parameters as for the OH stretching vibration, with the only difference that the carrier frequency is changed to Ω = 1920 cm^{-1}.

The reaction coordinates are mainly excited, but the harmonic degrees of freedom also accept part of the energy, Fig. 4.23 Panel (A). However, not all skeleton modes have equal importance. In particular, mode ν_{26} gets significantly excited. The out of phase oscillations of E_{xy} and $E_{\nu_{26}}$ imply energy exchange between the reaction coordinates and this mode. Considerable amount of energy flows into modes ν_{14} and ν_{30}, whereas modes ν_4 and ν_6 only get slightly excited.

Concerning the population changes, Fig. 4.23 Panel (B), the excitation of the OD stretching vibration is marked by population transfer between the ground state and the stretching level $|\alpha = 3\rangle$. Nevertheless, the OD bending mode $|\alpha = 2\rangle$ gets excited, but also the overtones of the bending $|\alpha = 4\rangle$ and the stretching modes $|\alpha = 7\rangle$ get populated via one and two photon transitions, respectively. It is important to note that significant population of the stretching mode persists even after 5 ps, Fig. 4.24, although the amplitude of the oscillations slowly decreases in time. The estimated IVR time is close to 3 ps.

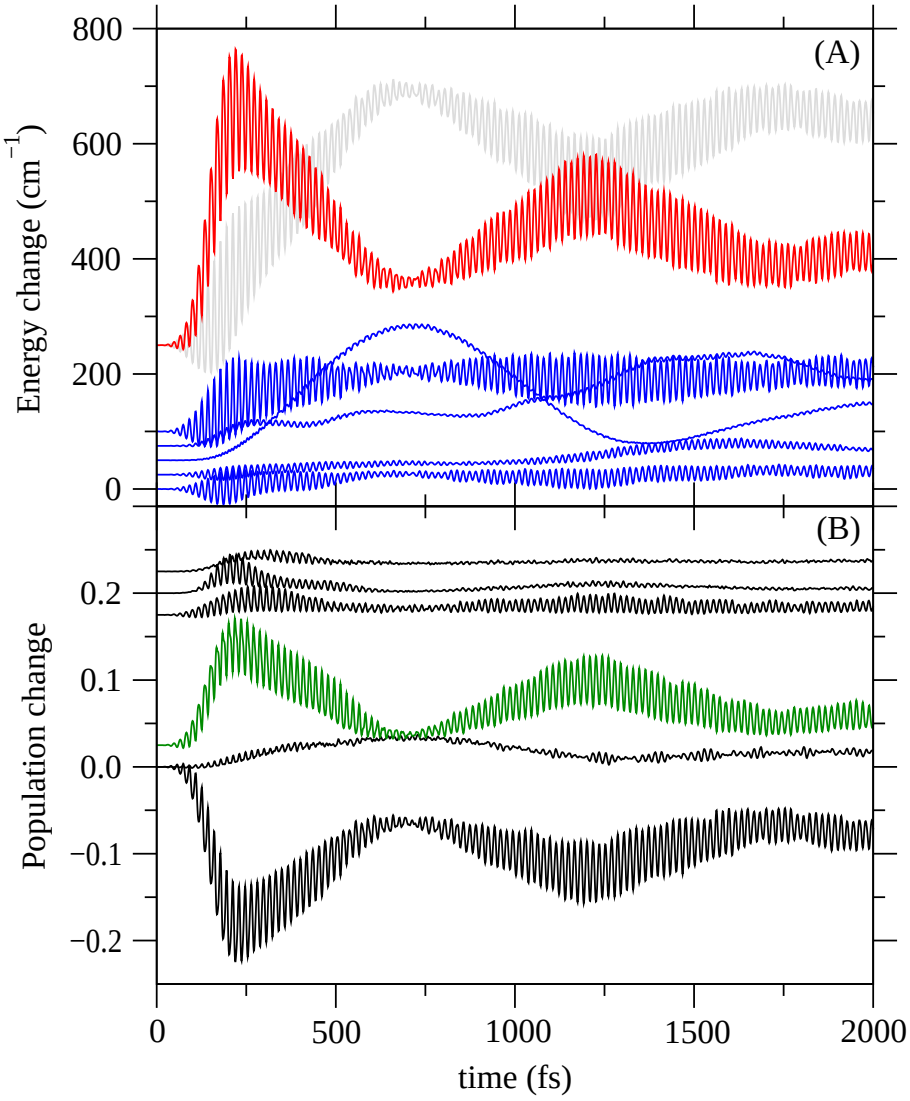

Figure 4.23: (A) Energy change with respect to time zero for the two reaction coordinates, E_{xy} (red line), $\sum_i E_{\nu_i}$ (grey line) and the five uncoupled normal modes, $E_{\nu_{14}}$, $E_{\nu_{30}}$, $E_{\nu_{26}}$, E_{ν_6}, E_{ν_4} (blue lines, from top, the curves are vertically offset). (B) Population change of the diabatic states with respect to time zero: ΔP_1, P_2, P_3, P_4, P_7 and $\sum_{\alpha=5,6,8-10} P_\alpha$, (curves from bottom to top, the upper curve vertically offset).

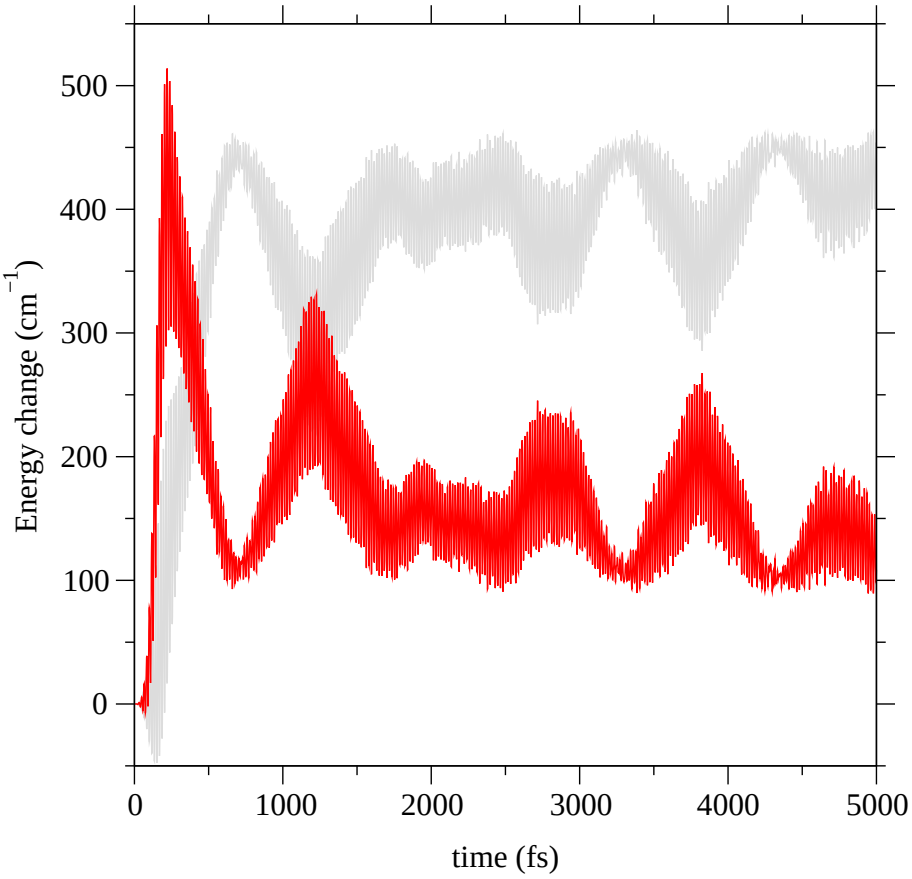

Figure 4.24: Energy change with respect to time zero for the two reaction coordinates, E_{xy} (red line), $\sum_i$ and E_{ν_i} (grey line) from a 5 ps propagation.

Comparison of the OH and the OD Stretching Dynamics

It has been shown that skeleton modes have different influence on the dynamics of the hydrogen and the deuterium atom. However, comparing the energy changes we note that in both cases mode ν_{26} plays a significant role. In addition, $E_{\nu_{26}}$ reaches its maximum after the pulse had been turned off. This means that due to its coupling to the reaction coordinates, ν_{26} becomes excited directly.

Separate contributions to the total energy of mode ν_{26} are displayed in Fig. 4.25. Concerning the potential energy part, in both cases the $f_{26}Q_{26}$ term approximately averages to zero, and the part $1/2K_{26}Q_{26}^2$ is responsible for the energy changes. This means that the H/D motion mainly affects the force constant of mode ν_{26}, thereby directly influencing also the kinetic energy of this mode.

The common feature of the OH and OD stretching dynamics is that the two highest frequency modes, ν_{26} and ν_{30} couple most strongly to the H and D atoms. This was to be expected, since those two modes have the highest reorganization energy at the keto state, Table 4.6, and the stretching vibration actually promotes the molecule towards this structure.

The main difference between the OH and the OD stretching dynamics lies in the extent of possible energy redistribution. The dynamics of the OH stretching vibration is marked by fast internal vibrational redistribution and a significant influence of *all* five skeleton modes. On the other hand, the deuterated system retains quasi - coherent character even after 5 ps propagation, which might partly

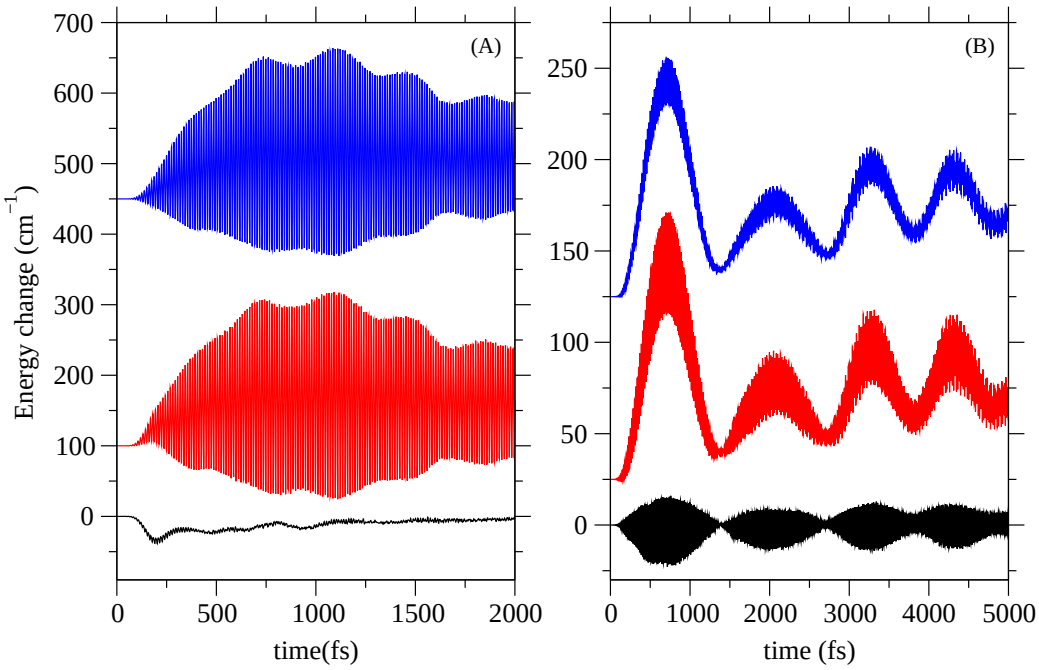

Figure 4.25: Different contributions to the total energy of the mode ν_{26} for SA-H (A) and SA-D (B). From bottom to top: fQ, $1/2KQ^2$, and the kinetic energy T.

be due to the fact that the two low frequency modes are not strongly involved in the deuterium dynamics, so there are fewer channels for the deuterium relaxation. This was to be expected in view of the IR spectra, Fig. 4.13 and 4.14: The simpler form of the SA-D spectrum in the ν_s region indicates less complex dynamics.

Expectation Values of the Reaction Coordinates

The expectation values of the reaction coordinates are displayed in Fig. 4.26. Since the energy level of the OH stretching vibration lies much higher than the one for the OH/OD bending mode, $\mathrm{H}_x(t)$ does not oscillate around the equilibrium position. That is, owing to the fact that the potential is shallower in the negative direction of the x axis, Fig. 4.9, the position of the hydrogen atom is on the average further away from the oxygen atom, as compared to the equilibrium structure. Also, the excitation in the x direction is, as supposed, more pronounced than in the y direction.

Concerning the deuterium motion, the OD stretching level is positioned deeper in the enol well, so the excitations in the positive and the negative directions of the x axis are almost the same. Nevertheless, $\Delta\mathrm{D}_y$ is positive due to the lower gradient of the potential in the $+y$ direction. Furthermore, the amplitude of the deuterium motion drastically decreases around 0.7, 3.3 and 4.3 ps. This centering

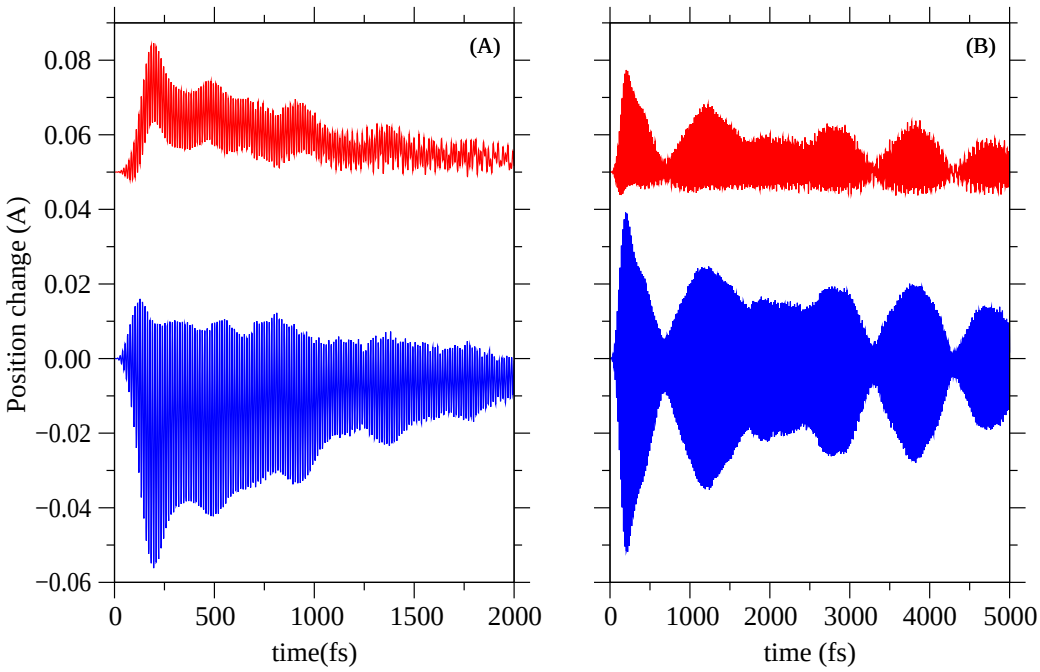

Figure 4.26: Position of the reactive atoms with respect to the equilibrium structure upon en excitation of the OH/OD stretching vibration is shown on the left/right Panel. Lower curves correspond to the motion in the x, and upper in the y direction.

coincides with the decrease of the amplitude of E_{xy}, Fig. 4.24. It is interesting to observe such focusing of the position expectation values, despite the complexity of the dynamics.

4.6 Comparison of AFF and CRS Results

In this chapter the properties of Salicylaldimine were investigated. Since the system possesses an intramolecular hydrogen bond, the PES was expected to have anharmonic character. Hence, two approaches that take into account anharmonicity were applied: the Anharmonic Force Field and the Cartesian Reaction Surface method. The AFF method is known to be suitable for describing processes that take place close to the equilibrium and in order to describe couplings between the modes all cubic and selected quartic anharmonic terms had been included in the Hamiltonian. However, the featureless region in the linear IR spectrum in the red part of the ν_s band indicated that the anharmonicity of the PES is very strongly pronounced, so in order to obtain a reliable characterization of the system it is necessary to include higher order anharmonic terms, especially with respect to the bending and the stretching motion which are related to the reaction coordinates for the proton transfer. Further, since the minimal number of degrees of freedom necessary for a satisfactory description is in this case rather large (nine) it turned out that for such strongly anharmonic systems the AFF approach is not appropriate. Therefore, we turned to a more general method, CRS, which not only allows more precise treatment of the dynamics close to the equilibrium, but also enables investigation of large amplitude motions of the reactive hydrogen atom.

It appears as if the diagonal terms can reproduce the position of the OH bending and stretching band. However, in this strongly anharmonic system these are no pure transitions and much of the substructure, in particular of the stretching band, is missing in the 4^{th} order force field.

Another important issue is the dimensionality of the models. The AFF model was composed of 9, and the CRS model of 7 degrees of freedom. Not all modes have the same importance: in the former case we focused on the OH bending and stretching vibration, whereas in the latter we considered large amplitude motions of the hydrogen atom in the x and y directions. However, it was necessary to include additional 7 and 5 harmonic vibrations, respectively. The difference in the nature of the additional modes lies in the fact that the *AFF modes* include the reactive hydrogen atom, while the *CRS modes* contain only the skeleton atoms. Therefore, the latter seem to be more flexible, i.e., the CRS picture is more compact. In order to compare the AFF and the CRS modes, we calculated the overlap of the normal mode vectors, which showed that modes ν_3^{AFF}, ν_{27}^{AFF} and ν_{32}^{AFF} approximately

correspond to ν_4^{CRS}, ν_{26}^{CRS} and ν_{30}^{CRS}, respectively. That is, for certain modes there is an almost one to one correspondence. However, modes ν_5^{AFF}, ν_7^{AFF}, ν_{12}^{AFF} and ν_{16}^{AFF} are combinations of ν_6^{CRS} and ν_{14}^{CRS} (compare Figures 4.5 and 4.8).

To summarize, the AFF approach is recommendable for systems which are not characterized by strong couplings between the degrees of freedom. But, if this is the case (like in SA), the CRS approach is more suitable, because: (i) it treats the anharmonicity of selected large amplitude motions more rigorously; (ii) it offers a more concise description; (iii) due to the larger number of AFF modes included, the numerical effort for the CRS method is not necessarily higher.

4.7 Would it be Possible to Control a Hydrogen Transfer Reaction?

In this section, we will address the possibility to control a hydrogen transfer reaction using the example of SA. Comparing the keto - like states of the normal species and the deuterated Salicylaldimine, the keto wave function of SA-D is much stronger localized in the keto well compared to the protonated molecule. Therefore, by considering just the zero - order keto states, it would probably be easier to obtain control over the deuterated species since it seems to provide a better target state.

In order to examine the stability of this target state (keto tautomer) in the spirit of the diabatic states, we followed a field - free propagation of an initially populated vibrational ground state with respect to the skeleton modes within the keto - diabatic level[2] $|\alpha = 10\rangle$, where all state and mode couplings have been turned off, Fig. 4.27. We included 15 diabatic states for this purpose. The number of single particle functions is compiled in Table 4.10. It ensures the smallest natural orbital

[2]This approach was suggested by M. Korolkov.

	diabatic state (α)														
mode	1	2	3	4	5	6	7	8	9	10	11	12	13	14	15
ν_4	7	6	5	5	5	4	4	4	4	4	4	3	3	1	1
ν_6	6	6	5	5	5	4	4	4	4	4	3	3	3	1	1
ν_{14}	7	6	5	5	5	4	4	4	3	3	3	3	3	1	1
ν_{26}	5	4	4	4	4	3	3	3	3	3	3	3	3	1	1
ν_{30}	5	4	4	4	4	3	3	3	3	3	3	3	3	1	1

Table 4.10: The number of single particle functions per diabatic state $|\alpha\rangle$ for the substrate modes.

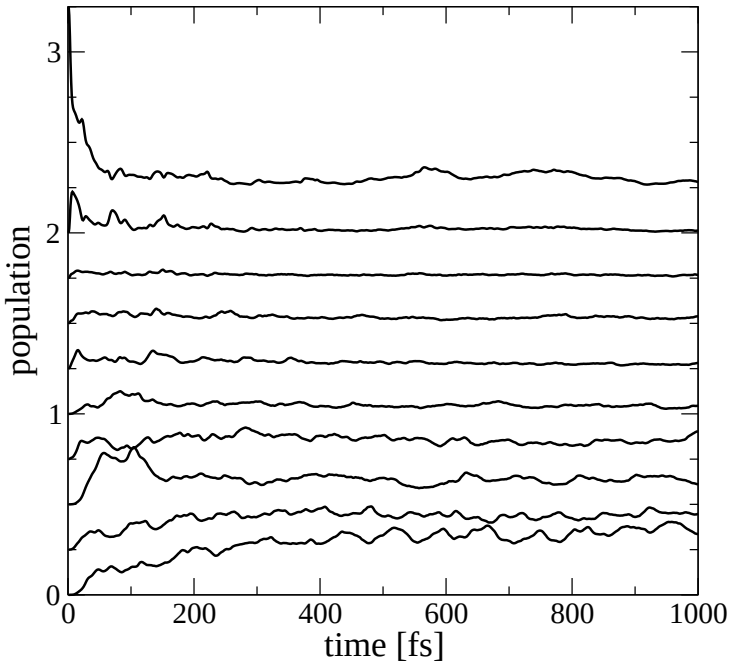

Figure 4.27: Population change after initial population of the keto - like state. Each curve is vertically offset by (α - 1)*0.25.

population to be below 1%. The grid dimensions are the same as in the previous calculations. The dynamics is marked by fast depopulation of the keto - like state within 50 fs. Significant transient population is characteristic for state $|\alpha = 9\rangle$, for example. However, the population is transferred mainly into four lowest states, in particular the OD stretching level $|\alpha = 3\rangle$ is appreciably populated within the first 170 fs. Finally, the system relaxes to the ground state - after 1 ps the diabatic ground state shows population of about 30 %. However, at the end of the propagation a considerable amount of population (5 - 10 %) persists in the initial state, which confirms its relative stability. Those results show that the relaxation mechanism proceeds via lower lying levels, with the $|\alpha = 3\rangle$ state playing an important role, so a crude pathway including only the most important steps can be sketched as

$$|\alpha = 10\rangle \rightarrow |\alpha = 3\rangle \rightarrow |\alpha = 1\rangle$$

as shown in Fig. 4.29 below, Panel (A). Apparently, a direct transition to the ground state surface does not take place because: (i) the overlap of the initial and the ground state wave functions is small; (ii) the couplings between the keto and the intermediate states are rather pronounced.

The energy changes of the uncoupled modes, Fig. 4.28, demonstrate that they have more or less equal contribution in the deuterium dynamics, apart from the fact that modes with higher frequencies accept larger amount of energy. This means

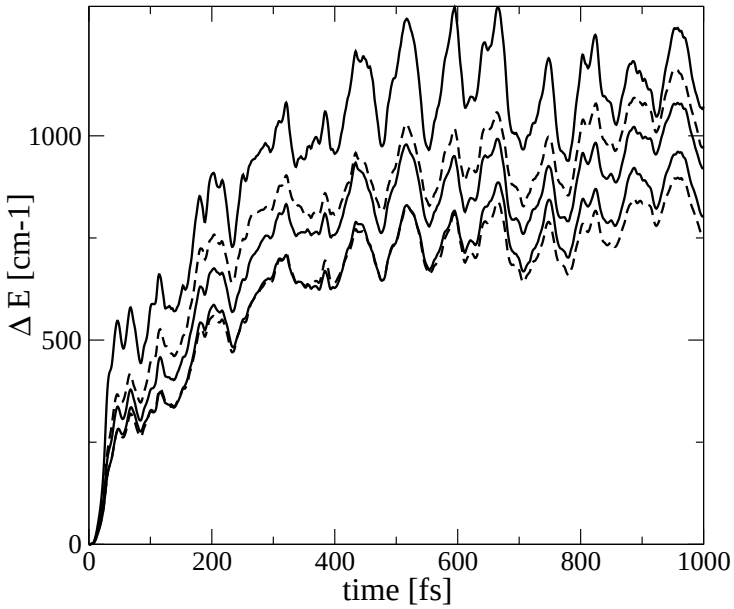

Figure 4.28: Energy change of the uncoupled substrate modes after the initial population of the keto - like state. The curves correspond to (from bottom on the right side) ν ν_6 (dashed), ν_4 (solid), ν_{26} (solid), ν_{30} (dashed), ν_{14} (solid).

that the nature of the modes, i.e., their division into promoting and linear coupling type is not of relevance for the considered deuterium transfer reaction.

The relaxation dynamics revealed the strength of couplings between the diabatic levels. This knowledge is useful if one would be interested in the reverse process, i.e., starting from the global minimum and reaching the keto state. Since we are interested in the dynamics initiated by means of IR laser pulses, it is instructive to study an already developed approach that deals with double minimum systems, namely a Tannor - Rice like mechanism [22] which rests on application of two pulses [98], [108]. The first *pump* pulse excites the molecule from the ground state to a vibrationally excited state that lies above the barrier. The second *dump* pulse stimulates the deexcitation of the wave packet into the other minimum. This method has been shown to be suitable for low - dimensional systems which are not characterized by strong intramolecular couplings. In addition, those results correspond to low excitations, that is to the two lowest excited states and the states that are located above the barrier are likely to be also marked by strong couplings. However, the deuterium dynamics discussed in Section 4.5 brings out appreciable couplings of the SA skeleton to the deuterium motion. This makes the Tannor - Rice like pump - dump mechanism not suitable for the present model. It is necessary to find a pathway that involves low energy excitations. The relaxation mechanism which precedes via an intermediate state suggests a possible pathway for the process in the opposite direction. In the simplest way, one could consider ap-

plication of two plain pulses. The first pulse should prepare the molecule for the final transformation. Actually, the motion of the deuterium atom during the OD stretching vibration is easily acceptable, since the reactive atom gets a momentum in the right direction, i.e., towards the keto well. The second pulse should localize the wave packet in the keto well. This simple two - pulse control scheme is depicted in Fig, 4.29, Panel B. Our calculations in Section 4.5 preformed with sin^2 pulses show that the deuterium motion cannot be considered as being uncoupled from the substrate vibrations and that this interaction causes energy redistribution among all DOFs. Therefore, in order to obtain significant amount of the product it is necessary to employ shaped pulses that would not only transfer the wave packet over the barrier, but also localize it in the keto - well. Recent advances in the field of optimal control encourage further research in this direction.

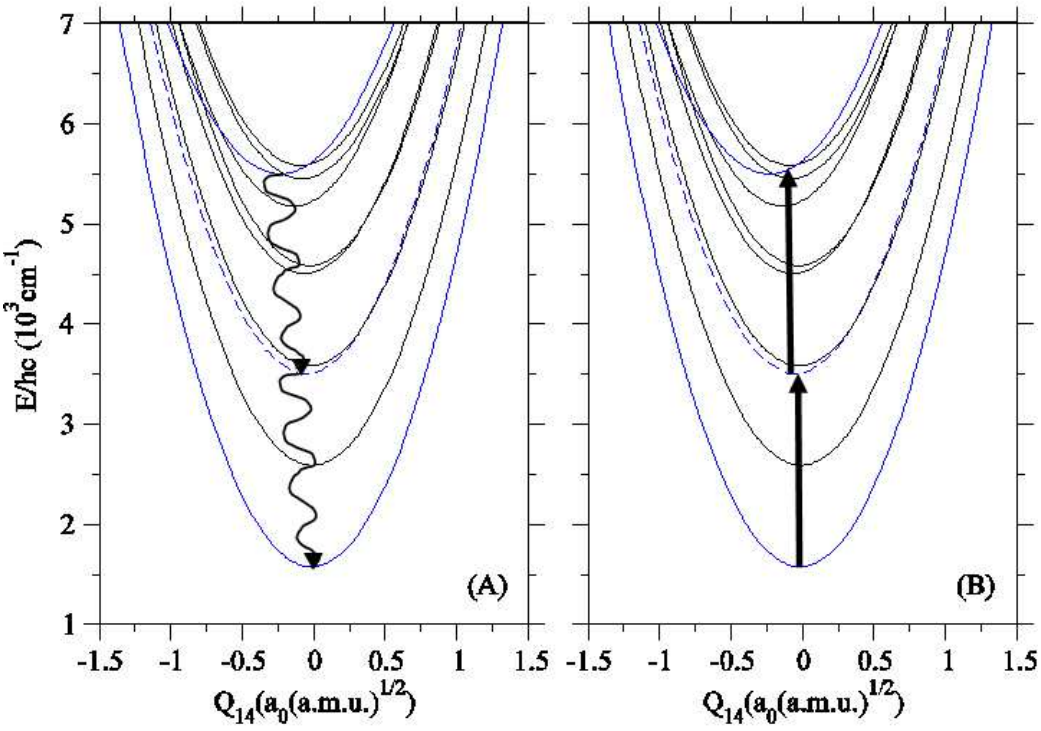

Figure 4.29: Diabatic potential energy curves for mode ν_{14}. The lower and the upper blue line correspond to the ground and the keto - like state. The dashed line represents state $|\alpha = 3\rangle$. (A) Relaxation pathway from the keto - like state. (B) Proposed mechanism for the control of enol - keto tautomerization.